Linear Sampling Method applied to Non Destructive Testing of an elastic waveguide: theory, numerics and experiments

Vahan Baronian, Laurent Bourgeois, Bastien Chapuis, Arnaud Recoquillay

Linear Sampling Method applied to Non Destructive Testing of an elastic waveguide: theory, numerics and experiments

Vahan Baronian[a], Laurent Bourgeois[b,*], Bastien Chapuis[a], Arnaud Recoquillay[a,b]

[a]*CEA, LIST, Gif-sur-Yvette, France*
[b]*Laboratoire POEMS, UMR ENSTA/CNRS/INRIA, ENSTA ParisTech, 828 Boulevard des Maréchaux, 91120 Palaiseau, France*

Abstract

This paper presents an application of the Linear Sampling Method to ultrasonic Non Destructive Testing of an elastic waveguide. In particular, the NDT context implies that both the solicitations and the measurements are located on the surface of the waveguide and are given in the time domain. Our strategy consists in using a modal formulation of the Linear Sampling Method at multiple frequencies, such modal formulation being justified theoretically in [1] for rigid obstacles and in [2] for cracks. Our strategy requires the inversion of some emission and reception matrices which deserve some special attention due to potential ill-conditioning. The feasibility of our method is proved with the help of artificial data as well as real data.

Keywords: Elastic waveguide, Inverse scattering problem, Linear Sampling Method, Lamb modes, Experimental data.

1. Introduction

This paper presents a Non Destructive Testing method to identify some defects in an elastic waveguide. Such a subject is far from being original, but the novelty of our contribution is that we apply a rather mathematical approach of inverse problems, namely the Linear Sampling Method, to improve the ultrasonic inspection of elastic waveguide structures from real data. In particular, at the end of the paper we present some promising identification results obtained with experimental data. There is a huge amount of works dealing with NDT experimental ultrasonic techniques for waveguides such as metallic plates or pipes. But NDT ultrasonic techniques have limitations: some of them take the modal decomposition of the waves into account, which allows the inspection

---

of a wide area. But these techniques need to track the propagation of a single guided mode at a low frequency, which is difficult in practice [3, 4, 5, 6, 7, 8]. Moreover, the guided-wave based techniques often depend on the type of defect which is expected, that is a void, a crack or some corrosion. Other techniques do not take the modal decomposition of the waves into account and enable the inspection, at a high frequency, of a limited area which is close to the sensor [9, 10]. Our aim is to image an elastic waveguide in a wide area and at a high frequency, using all the propagating modes at the same time. Furthermore, we wish to conceive a method which does not depend on the number and the type of defects that are likely to be detected. A sampling method such as the Linear Sampling Method has all these nice features, provided we manage to adapt it to the constraining context of NDT.

The Linear Sampling Method has now a long history since its introduction in [11] in the free space configuration and for the acoustic case. It consists, for each sampling point z describing a grid, to check if some appropriate and analytically known test function depending on z belongs or not to the range of a linear operator the definition of which is based on the data. In the case of a positive answer, the point z belongs to the defect, which is a practical way of retrieving its boundary. Since the nineties, the LSM has been widely used in other configurations and for other types of physical settings. For example, both for penetrable or impenetrable objects, the LSM was extended to elasticity in [12, 13] and to electromagnetism in [14, 15]. In the acoustic case, the LSM was adapted to the waveguide geometry in [16, 17, 18, 19]. The case of elastic waveguides was addressed in [1], the case of electromagnetic waveguides in [20]. Given the importance of cracks in NDT, we mention that the LSM was adapted to the detection of cracks in [21, 22] in the case of acoustics and in [2, 23] in the case of elasticity. To complete this short review of the Linear Sampling Method, while the previous contributions consider waves in the frequency domain, we point out that a time domain version of the LSM was developed in [24] and adapted to waveguides in [25].

In almost all papers cited above, the LSM was applied to artificial data which somehow can be considered as ideal. In [1, 2, 17, 25], for instance, the sources and the receivers are located along transverse sections of the waveguide, which is not realistic in the context of Non Destructive Testing, where the sources and the receivers are both located on the surface of the waveguide. Furthermore, [1, 2, 17] stick to the frequency regime, while data are produced in the time domain in practice. The work we propose in elasticity is the same as we did in [26] in the acoustic case starting from [18]: handling surface data in the time domain in order to be in the exact conditions of a true experiment. An important contribution in [1, 2, 18] was that a modal formulation of the Linear Sampling Method, which is specific to waveguides, was introduced. Indeed, the term "modal formulation" refers to the fact that all the incident and scattered fields, in the region of the waveguide where there is no defect, can be decomposed along the guided modes. This decomposition enables us to select, among all modal amplitudes of the incident and scattered fields, those which correspond to the propagating part, that is the part which propagates at long distance without

2

attenuation. The remainder of the modal amplitudes is simply dropped. The advantage of such technique, which is justified in the acoustic case in [18], is that it regularizes, in a very efficient way, the ill-posed LSM equation to solve for each sampling point. In addition, our modal approach enables us to optimize the number of the sources/receivers and the spacing between them. Note that such optimization is significantly more difficult in the case of elasticity than in the case of acoustics, due to much higher complexity of the dispersion curves. Like in [26], our strategy is the following. Firstly, we transform the time domain data into multi-frequency data with the help of the Fourier transform. Secondly, at each frequency we transform the surface data into a novel set of ideal data which are suitable for the modal formulation of the LSM. Thirdly, we combine all the images given by the LSM at each frequency in order to obtain the best possible defect identification. The Linear Sampling Method in the frequency domain for an elastic waveguide is already justified for a Dirichlet obstacle in [1] and for cracks in [2]. The justification for a Neumann obstacle would follow the same lines and the justification for a penetrable obstacle would be very close to that of [27] for the periodic acoustic waveguide. It is important to note that our article does not provide any new result in this direction. Instead, it is focused on the application of the LSM in the presence of real data (in particular, surface data in the time domain) and on how the substantial issues generated by those real data can be fixed. To our best knowledge, proving the feasibility of the LSM with the help of real experiments on an elastic waveguide is new.

The outline of our paper is the following. Our Non Destructive Testing problem is described in section 2. In section 3, we briefly introduce the framework of mixed $\mathbf{X}, \mathbf{Y}$ variables, which is a key tool in view of the modal formulation of the Linear Sampling Method. In section 4, we summarize such modal formulation and its far field approximation. Section 5 details the way, starting from surface data in the time domain, we can handle those data in order to come back to the previous modal formulation. The section 6 is dedicated to some numerical experiments with artificial data, while section 7 presents our experimental setup and the corresponding identification results. Some conclusions are given in section 8. Lastly, in appendix A we derive the fundamental solution of the elastic waveguide for a Dirac located on its boundary, while the appendix B is an analysis of the cases when the matrix of modes introduced in section 5 is not invertible.

2. Setting of the problem

We consider a 2D waveguide $W = S \times \mathbb{R}$ for $S = (0, d)$ and $d > 0$ is the height of the waveguide. We denote (x_1, x_3) the coordinates of a generic point of W in the orthonomal basis $(\mathbf{e}_1, \mathbf{e}_3)$, x_3 being the coordinate of the infinite direction of the waveguide. The boundary of W is denoted $\Gamma = \Gamma_0 \cup \Gamma_d$, where Γ_0 (resp. Γ_d) corresponds to $x_1 = 0$ (resp. $x_1 = d$). This 2D configuration can also be viewed as a 3D configuration, such that if (x_1, x_2, x_3) are the three spatial coordinates, the waveguide is infinite in both directions x_2 and x_3 with invariance of all quantities with respect to x_2. This will coincide with the configuration of our

experimental device in section 7. In what follows, all vectors in $\mathbb{R}^2$ will be marked in bold characters while scalars and matrices will appear normally. For instance, $\mathbf{v}$ will denote the displacement, ε and σ the strain and stress tensors, respectively. We recall that, in the case of linear and isotropic elasticity, they are linked by

$$\varepsilon(\mathbf{v}) = \frac{\nabla \mathbf{v} + \nabla \mathbf{v}^T}{2}, \quad \sigma(\mathbf{v}) = \lambda \operatorname{tr}[\varepsilon(\mathbf{v})]\mathrm{Id}_2 + 2\mu\, \varepsilon(\mathbf{v}),$$

where m^T, $\operatorname{tr}(m)$ denote the transpose and the trace of the matrix m, respectively, Id_2 denotes the identity matrix, while λ and μ are the Lamé constants, which satisfy $\lambda + 2\mu > 0$ and $\mu > 0$.

We now consider a compactly supported scalar function φ of x_3 and a smooth (at least C^1) compactly supported scalar function χ of time t, with $\operatorname{supp}(\chi) \subset [0, +\infty)$. For some impenetrable obstacle D such that $\overline{D} \subset W$, let us denote $\Omega = W \setminus \overline{D}$ and assume that Ω is connected. We consider the displacement solution $\mathbf{v}$ in $\Omega \times (0, +\infty)$ to the scattering problem with Dirichlet boundary condition on ∂D:

$$\begin{cases} \rho \partial_t^2 \mathbf{v} - \operatorname{div}(\sigma(\mathbf{v})) & = & 0 & \text{in } \Omega \times (0, +\infty) \\ \sigma(\mathbf{v})\,\boldsymbol{\nu} & = & \varphi\,\chi \mathbf{e}_1 & \text{on } \Gamma_d \times (0, +\infty) \\ \sigma(\mathbf{v})\,\boldsymbol{\nu} & = & 0 & \text{on } \Gamma_0 \times (0, +\infty) \\ \mathbf{v} & = & 0 & \text{on } \partial D \times (0, +\infty) \\ \mathbf{v} & = & 0 & \text{on } \Omega \times \{0\} \\ \partial_t \mathbf{v} & = & 0 & \text{on } \Omega \times \{0\}, \end{cases} \tag{1}$$

where ρ is the density of the material and $\boldsymbol{\nu}$ is the outward unit normal to Ω. It should be noted that $\boldsymbol{\nu} = \mathbf{e}_1$ on Γ_d and $\boldsymbol{\nu} = -\mathbf{e}_1$ on Γ_0. Let us introduce two scalar functions f and g that are both compactly supported and even. While the function of time χ is given once and for all, the function of space φ is alternatively chosen as

$$\varphi(x_3) = f(x_3 - x_3^{s\pm}), \tag{2}$$

for several source locations $x_3^{s\pm}$. We denote by $\mathbf{v}^i$ the solution to the same problem as (1) in W without the boundary condition on ∂D and $\mathbf{v}^s = \mathbf{v} - \mathbf{v}^i$. In the classical terminology of scattering problems, $\mathbf{v}$ is the total field while $\mathbf{v}^i$ is the incident field and $\mathbf{v}^s = \mathbf{v} - \mathbf{v}^i$ is the scattered field. The measurements are given for all time $t \in (0, +\infty)$, for several receiver locations $x_3^{r\pm}$, by

$$\gamma(x_3^{r\pm}, t) = \int_{\mathbb{R}} g(x_3 - x_3^{r\pm})\mathsf{v}_1^s(d, x_3, t)\, dx_3, \tag{3}$$

where v_1^s is the component of the displacement $\mathbf{v}^s$ along $\mathbf{e}_1$. We assume that the position of sources and receivers are given by

$$x_3^{m\pm} = \pm(R + m\delta), \quad m = 0, \ldots, M - 1, \tag{4}$$

where $R > 0$ is such that the obstacle D is a priori located between the transverse sections of coordinates $x_3 = -R$ and $x_3 = R$ and $\delta > 0$. The well-posedness
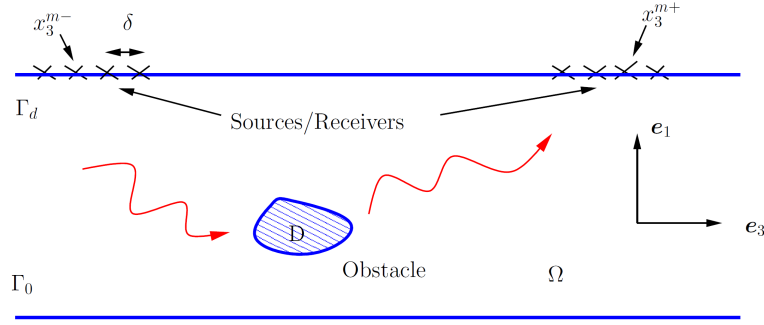
4

Figure 1: Configuration of the inverse problem

of the forward problem (1) for some data (φ, χ), which can be analyzed with classical tools like the J.-L. Lions Theorem or the Hille-Yosida Theorem (see [28]), will not be discussed in the present paper. The inverse problem consists in identifying the obstacle D in two situations:

- the full-scattering situation, that is we use the sources and receivers at x_3^{m+} and x_3^{m-} given by (4) for $m = 0, \ldots, M - 1$, which amounts to $2M$ sources and $2M$ receivers,

- the back-scattering situation, that is we use the sources at x_3^{m-} and the receivers at x_3^{m-} for $m = 0, \ldots, M - 1$, which amounts to M sources and M receivers.

In the full-scattering situation, both sides of the defect are accessible, while only one side is accessible in the back-scattering situation. The configuration of our inverse problem is illustrated in figure 1. In the inverse problem that we consider, the obstacle D is characterized by a Dirichlet boundary condition $\mathbf{v} = 0$ on ∂D for simplicity, like in [1]. But all the justifications remain valid for the Neumann boundary condition $\sigma(\mathbf{v}) \boldsymbol{\nu} = 0$ on ∂D or $\sigma(\mathbf{v}) \boldsymbol{\nu} = 0$ on both sides of a non closed curve, which model a void or a crack, respectively, like those we look for in the real experiment. We introduced the functions f and g in order to make the data of the inverse problem closer to the real data. Indeed, a Dirac Distribution would correspond for f to a punctual force applied at point $x_3^{r\pm}$ and for g to a punctual measurement of the displacement at point $x_3^s\pm$, while in practice using piezoelectric transducers leads us to impose a distributed force around $x_3^{r\pm}$ and to measure a weighted displacement around $x_3^s\pm$. Lastly, in our inverse problem, we impose a pressure force (along $\mathbf{e}_1$) on the boundary of the waveguide and measure the transverse displacement (along $\mathbf{e}_1$) on such boundary, because this is what is usually done in experiments and what we actually do in section 7. In fact, the theory developed in the present article enables us to consider other configurations (see [29]), for example a shear force (along $\mathbf{e}_3$) on the boundary and the axial displacement (along $\mathbf{e}_3$).

5

3. The **X**, **Y** variables

In this section we briefly summarize the results given in [30].

3.1. The guided modes

Let us introduce the **X** and **Y** variables, which is a useful tool in order to study the guided modes. They are defined from the displacement field **u** as

$$\mathbf{X} = \begin{pmatrix} t_1 \\ u_3 \end{pmatrix} \quad \text{and} \quad \mathbf{Y} = \begin{pmatrix} u_1 \\ t_3 \end{pmatrix},$$

where $\mathbf{u} = (u_1, u_3)$ and $\sigma(\mathbf{u})\mathbf{e}_3 = (t_1, -t_3) := (\sigma_{31}, \sigma_{33})$. These variables **X** and **Y**, which mix some components of the displacement and some components of the stress tensor, were introduced in [31] and revisited in [30, 32]. The main advantage of those variables is that, contrary to the displacement field **u**, its **X** and **Y** extensions can be decomposed in a complete basis of any transverse section of the waveguide, as we will see later. In our elastic waveguide, for a given fixed frequency ω, the so-called guided modes are the solutions **u**, with separate dependance on x_1 and x_3, to the system

$$\begin{cases} \operatorname{div}\sigma(\mathbf{u}) + \rho\,\omega^2 \mathbf{u} = 0 & \text{in} \quad W, \\ \sigma(\mathbf{u})\boldsymbol{\nu} = 0 & \text{on} \quad \Gamma. \end{cases} \tag{5}$$

It can be proved (see [30]) by using the **X**, **Y** variables that the system (5) is equivalent to the "evolution" problem with respect to the coordinate x_3:

$$\begin{cases} \dfrac{\partial}{\partial x_3}\begin{pmatrix} \mathbf{X} \\ \mathbf{Y} \end{pmatrix} = \begin{pmatrix} 0 & F_Y \\ F_X & 0 \end{pmatrix}\begin{pmatrix} \mathbf{X} \\ \mathbf{Y} \end{pmatrix} & \text{in} \quad W, \\ \sigma_{11}(\mathbf{Y}) = 0 & \text{on} \quad \Gamma, \\ t_1 = 0 & \text{on} \quad \Gamma, \end{cases} \tag{6}$$

where the transverse operators F_X and F_Y are defined by

$$F_Y\mathbf{Y} = \begin{pmatrix} -\partial_{x_1}\sigma_{11}(\mathbf{Y}) - \rho\,\omega^2 u_1 \\ -\alpha\,\partial_{x_1} u_1 - \dfrac{\alpha}{\lambda} t_3 \end{pmatrix} \quad \text{and} \quad F_X\mathbf{X} = \begin{pmatrix} \dfrac{t_1}{\mu} - \partial_{x_1} u_3 \\ \partial_{x_1} t_1 + \rho\,\omega^2 u_3 \end{pmatrix}, \tag{7}$$

with

$$\sigma_{11}(\mathbf{Y}) = 2\mu(1+\alpha)\partial_{x_1} u_1 - \alpha\,t_3, \quad \alpha = \lambda/(\lambda + 2\mu). \tag{8}$$

The guided modes are obtained by searching solutions to problem (6) in the form

$$\begin{pmatrix} \mathbf{X}(x) \\ \mathbf{Y}(x) \end{pmatrix} = \begin{pmatrix} \boldsymbol{\mathcal{X}}(x_1) \\ \boldsymbol{\mathcal{Y}}(x_1) \end{pmatrix} e^{i\beta x_3}$$

with $\beta \in \mathbb{C}$, which amounts to

$$\begin{cases} i\beta\begin{pmatrix} \boldsymbol{\mathcal{X}} \\ \boldsymbol{\mathcal{Y}} \end{pmatrix} = \begin{pmatrix} 0 & F_Y \\ F_X & 0 \end{pmatrix}\begin{pmatrix} \boldsymbol{\mathcal{X}} \\ \boldsymbol{\mathcal{Y}} \end{pmatrix} & \text{in} \quad S, \\ \sigma_{11}(\boldsymbol{\mathcal{Y}}) = 0 & \text{for} \quad x_1 \in \{0, d\}, \\ t_1 = 0 & \text{for} \quad x_1 \in \{0, d\}. \end{cases} \tag{9}$$

6

By using the spectral properties of the operators F_X and F_Y (see [30]) we obtain a discrete family of guided modes depending on $n \in \mathbb{N}$, given either in the $\mathbf{X}, \mathbf{Y}$ variables or in the $\mathbf{u}$ variable, by:

$$\left(\begin{array}{c} \mathbf{X}_n^{\pm}(x) \\ \mathbf{Y}_n^{\pm}(x) \end{array} \right) = \left(\begin{array}{c} \pm \boldsymbol{\mathcal{X}}_n(x_1) \\ \boldsymbol{\mathcal{Y}}_n(x_1) \end{array} \right) e^{\pm i \beta_n x_3}, \quad \mathbf{u}_n^{\pm}(x) = \left(\begin{array}{c} u_1^n(x_1) \\ \pm u_3^n(x_1) \end{array} \right) e^{\pm i \beta_n x_3}. \quad (10)$$

In 2D, the guided modes defined above are also known in the literature as the Lamb modes. In practice, for some given ω, the β_n do not have an analytical expression. The dispersion relation that they satisfy, as well as the corresponding displacement (u_1^n, u_3^n) are specified in appendix B. An essential result (see [30]) concerning these guided modes is the following biorthogonality relationship, for $m, n \in \mathbb{N}$:

$$(\boldsymbol{\mathcal{X}}_n | \boldsymbol{\mathcal{Y}}_m)_S = \delta_{nm} J_n$$

for some constant J_n, where the bilinear form $(\cdot | \cdot)_S$ is defined for $\boldsymbol{\mathcal{X}} = (t_1, u_3)^T$ and $\boldsymbol{\mathcal{Y}} = (u_1, t_3)^T$ in $\mathbf{L}^2(S) = (L^2(S))^2$ by

$$(\boldsymbol{\mathcal{X}} | \boldsymbol{\mathcal{Y}})_S = \int_0^d (\mathcal{X}_1 \mathcal{Y}_1 + \mathcal{X}_3 \mathcal{Y}_3) \, ds = \int_0^d (t_1 \, u_1 + u_3 \, t_3) \, ds. \quad (11)$$

The bilinear form (11) can be extended by duality to the case when $\boldsymbol{\mathcal{X}} \in \tilde{H}^{-\frac{1}{2}}(S) \times H^{\frac{1}{2}}(S)$ and $\boldsymbol{\mathcal{Y}} \in H^{\frac{1}{2}}(S) \times \tilde{H}^{-\frac{1}{2}}(S)$, where $\tilde{H}^{-\frac{1}{2}}(S)$ is the dual space of $H^{\frac{1}{2}}(S)$. The following assumption is made in the sequel.

Assumption 1. *The frequency ω is such that none of the β_n vanishes and none of the elements of the family $(\boldsymbol{\mathcal{X}}_n, \boldsymbol{\mathcal{Y}}_n)$ satisfies $(\boldsymbol{\mathcal{X}}_n | \boldsymbol{\mathcal{Y}}_n)_S = 0$.*

Assumption 1 eliminates the possibility of infinite phase velocity and of vanishing group velocity (see [33]). Such assumption enables us to set $J_n = 1$ for all $n \in \mathbb{N}$. From the numerical results, Assumption 1 seems to be violated for at most a countable set of frequencies ω. The guided modes for which β_n is purely real are said to be propagating, since they propagate at long distance without attenuation. The guided modes can then be organized in two families:

- the rightgoing modes $(\beta_n, \boldsymbol{\mathcal{X}}_n, \boldsymbol{\mathcal{Y}}_n)$ for $n \in \mathbb{N}$, which correspond to $\text{Im}(\beta_n) > 0$ (for non-propagating modes) or $\frac{\partial \omega}{\partial \beta_n} > 0$ (for propagating modes), where ω is an implicit function of β_n via the dispersion relation (60).

- the leftgoing modes $(-\beta_n, -\boldsymbol{\mathcal{X}}_n, \boldsymbol{\mathcal{Y}}_n)$ for $n \in \mathbb{N}$.

It should be noted that the non-propagating modes are either evanescent (β_n is purely imaginary) or inhomogeneous (β_n is not purely imaginary). Without loss of generality, we assume that the propagating modes are ordered in such a way that the sequence of β_n decreases with respect to n.

3.2. The radiation condition

Let us assume the following conjecture.

7

Conjecture 2. *For every* $\boldsymbol{\mathcal{X}} \in \tilde{H}^{-\frac{1}{2}}(S) \times H^{\frac{1}{2}}(S)$ *we have*

$$\boldsymbol{\mathcal{X}} = \sum_{n \in \mathbb{N}} (\boldsymbol{\mathcal{X}}|\boldsymbol{\mathcal{Y}}_n)_S \boldsymbol{\mathcal{X}}_n, \tag{12}$$

for every $\boldsymbol{\mathcal{Y}} \in H^{\frac{1}{2}}(S) \times \tilde{H}^{-\frac{1}{2}}(S)$ *we have*

$$\boldsymbol{\mathcal{Y}} = \sum_{n \in \mathbb{N}} (\boldsymbol{\mathcal{X}}_n|\boldsymbol{\mathcal{Y}})_S \boldsymbol{\mathcal{Y}}_n, \tag{13}$$

and there exists $C > 0$ such that

$$\sum_n |(\boldsymbol{\mathcal{X}}|\boldsymbol{\mathcal{Y}}_n)_S|^2 \leq C \, \|\boldsymbol{\mathcal{X}}\|^2_{\tilde{H}^{-\frac{1}{2}}(S) \times H^{\frac{1}{2}}(S)}$$

$$\sum_n |(\boldsymbol{\mathcal{X}}_n|\boldsymbol{\mathcal{Y}})_S|^2 \leq C \, \|\boldsymbol{\mathcal{Y}}\|^2_{H^{\frac{1}{2}}(S) \times \tilde{H}^{-\frac{1}{2}}(S)}.$$

215 *Decompositions (12) and (13) are also true for $\boldsymbol{\mathcal{X}}$ and $\boldsymbol{\mathcal{Y}}$ in $\mathsf{L}^2(S)$.*

To our best knowledge, a rigorous proof of the above completeness result, which seems true according to all our numerical experiments, does not exist. Following [30], from conjecture 2 the family $(\beta_n, \boldsymbol{\mathcal{X}}_n, \boldsymbol{\mathcal{Y}}_n)$ enables us to define a continuous $\boldsymbol{\mathcal{Y}}$-to-$\boldsymbol{\mathcal{X}}$ operator T acting on a transverse section S, precisely

$$T : \left(\begin{array}{c} H^{\frac{1}{2}}(S) \times \tilde{H}^{-\frac{1}{2}}(S) \to \tilde{H}^{-\frac{1}{2}}(S) \times H^{\frac{1}{2}}(S) \\ \boldsymbol{\mathcal{Y}} \mapsto \sum_{n \in \mathbb{N}} (\boldsymbol{\mathcal{X}}_n|\boldsymbol{\mathcal{Y}})_S \boldsymbol{\mathcal{X}}_n \end{array} \right). \tag{14}$$

220 It is shown in [30] that the radiation condition in the elastic waveguide can be imposed by restricting the scattering problem to a bounded domain W_R located between a right transverse section $S_R = S \times \{R\}$ and a left transverse section S_{-R} and by prescribing the boundary conditions $T_+\mathbf{Y} = \mathbf{X}$ on S_R and $T_-\mathbf{Y} = -\mathbf{X}$ on S_{-R}, where T_+ and T_- are acting on sections S_R and S_{-R}, 225 respectively. In what follows, Γ_R is the portion of Γ delimited by the sections S_{-R} and S_R.

3.3. The fundamental solution

The classical outgoing Green solution of the elastic waveguide W, denoted by G_u^σ, is such that for $y \in W_R$, the 2×2 tensor $G_u^\sigma(\cdot, y)$ satisfies the problem:

$$\begin{cases} -\operatorname{div}\sigma(G_u^\sigma(\cdot, y)) - \rho\omega^2 G_u^\sigma(\cdot, y) = \delta(\cdot - y)\mathrm{Id}_2 & \text{in} \quad W_R \\ \sigma(G_u^\sigma(\cdot, y))\,\boldsymbol{\nu} = 0 & \text{on} \quad \Gamma_R \\ T_\pm G_Y^\sigma(\cdot, y) = \pm G_X^\sigma(\cdot, y) & \text{on} \quad S_{\pm R}, \end{cases} \tag{15}$$

230 where G_X^σ (resp. G_Y^σ) denotes the 2×2 tensors such that each line of G_X^σ (resp. G_Y^σ) is formed by the $\mathbf{X}$ extension (resp. $\mathbf{Y}$ extension) of the corresponding line of tensor G_u^σ. By using the coordinates of $\boldsymbol{\mathcal{X}}_n = (t_1^n, u_3^n)^T$ and $\boldsymbol{\mathcal{Y}}_n = (u_1^n, t_3^n)^T$, the tensor G_u^σ is given by

$$G_u^\sigma(x, y) = -\sum_{n \in \mathbb{N}} \left(\begin{array}{cc} u_1^n(x_1)u_1^n(y_1) & -s(x_3 - y_3)u_1^n(x_1)u_3^n(y_1) \\ s(x_3 - y_3)u_3^n(x_1)u_1^n(y_1) & -u_3^n(x_1)u_3^n(y_1) \end{array} \right) \frac{e^{i\beta_n|x_3 - y_3|}}{2},$$

8

where s is the sign function. As a useful tool to formulate the Linear Sampling Method in our elastic waveguide, we introduce the extended outgoing Green tensor G for the elastic waveguide already introduced in [1], which is well adapted to the $\mathbf{X}, \mathbf{Y}$ formalism. The 4×4 tensor G is such that for $y \in W_R$, $G(\cdot, y)$ is the solution to the problem:

$$
\begin{cases}
\dfrac{\partial}{\partial x_3} G(\cdot, y) = \begin{pmatrix} 0 & F_Y \\ F_X & 0 \end{pmatrix} G(\cdot, y) - \delta(\cdot - y) \begin{pmatrix} \mathrm{Id}_2 & 0_2 \\ 0_2 & \mathrm{Id}_2 \end{pmatrix} & \text{in} \quad W_R \\
\sigma_{11}(G_Y(\cdot, y)) = 0, \quad \mathsf{t}_1(G_Y(\cdot, y)) = 0 & \text{on} \quad \Gamma_R \\
T_\pm G_Y(\cdot, y) = \pm G_X(\cdot, y) & \text{on} \quad S_{\pm R}.
\end{cases}
\tag{16}
$$

Here, G_X and G_Y denote the $X-$rows and $Y-$rows of the matrix G, respectively. If we decompose the tensor G into four 2×2 blocks, that is

$$
G = \begin{pmatrix} G_X^X & G_X^Y \\ G_Y^X & G_Y^Y \end{pmatrix},
\tag{17}
$$

it is proved in [1] that these blocks can be specified as

$$
\begin{aligned}
G_X^X(x, y) &= -\sum_{n \in \mathbb{N}} s(x_3 - y_3) \boldsymbol{\mathcal{X}}_n(x_1) \otimes \boldsymbol{\mathcal{Y}}_n(y_1) \frac{e^{i\beta_n |x_3 - y_3|}}{2}, \\
G_X^Y(x, y) &= -\sum_{n \in \mathbb{N}} \boldsymbol{\mathcal{X}}_n(x_1) \otimes \boldsymbol{\mathcal{X}}_n(y_1) \frac{e^{i\beta_n |x_3 - y_3|}}{2}, \\
G_Y^X(x, y) &= -\sum_{n \in \mathbb{N}} \boldsymbol{\mathcal{Y}}_n(x_1) \otimes \boldsymbol{\mathcal{Y}}_n(y_1) \frac{e^{i\beta_n |x_3 - y_3|}}{2}, \\
G_Y^X(x, y) &= -\sum_{n \in \mathbb{N}} s(x_3 - y_3) \boldsymbol{\mathcal{Y}}_n(x_1) \otimes \boldsymbol{\mathcal{X}}_n(y_1) \frac{e^{i\beta_n |x_3 - y_3|}}{2}.
\end{aligned}
\tag{18}
$$

By selecting among the rows of matrix G those which correspond to the components of $\mathbf{u}$ and by selecting among the columns of G those which correspond to the components of $\sigma \, \mathbf{e}_3$ (we recall that $\sigma \, \mathbf{e}_3 = (\mathsf{t}_1, -\mathsf{t}_3)^T$), we obtain the classical Green tensor G_u^σ from the extended one. More generally and for simplicity, G_a^b will denote the tensor obtained from G by selecting among the rows of matrix G those which correspond to the components of type a and by selecting among the columns of G those which correspond to the components of type b.

4. The modal formulation of the Linear Sampling Method

We briefly summarize the modal formulation of the Linear Sampling Method such as described in [1] for rigid obstacles. But the justification can be easily adapted to the case of voids or cracks (see [2]). As recalled in the introduction, the method itself is independent of the nature of the defect.

9

We consider the following scattering forward problem : for $\mathbf{f} \in (H^{-\frac{1}{2}}(\partial D))^2$, find $\mathbf{u} \in (H^1(\Omega_R))^2$ such that

$$\begin{cases} \operatorname{div}\sigma(\mathbf{u}) + \rho\omega^2\mathbf{u} = 0 & \text{in} & \Omega_R, \\ \sigma(\mathbf{u})\,\boldsymbol{\nu} = 0 & \text{on} & \Gamma_R, \\ \mathbf{u} = \mathbf{f} & \text{on} & \partial D \\ T_{\pm}\mathbf{Y} = \pm\mathbf{X} & \text{on} & S_{\pm R}, \end{cases} \tag{19}$$

where $\Omega_R = W_R \setminus \overline{D}$. Let us denote by $u_Y^s(\cdot, y)$ the solution to problem (19) which corresponds to $f = -G_u^Y(\cdot, y)|_{\partial D}$ for $y \in \hat{S} := S_{-R} \cup S_R$ and by $X_Y^s(\cdot, y)$ the $\mathbf{X}$ extension of $u_Y^s(\cdot, y)$. Similarly, let us denote by $u_X^s(\cdot, y)$ the solution to problem (19) which corresponds to $f = -G_u^X(\cdot, y)|_{\partial D}$ for $y \in \hat{S}$ and by $Y_X^s(\cdot, y)$ the $\mathbf{Y}$ extension of $u_X^s(\cdot, y)$. We consider the inverse problem of finding the obstacle D from the trace on $\hat{S}$ of either $X_Y^s(\cdot, y)$ or $Y_X^s(\cdot, y)$, for all $y \in \hat{S}$. In order to solve it we introduce the near field operators N_X and N_Y defined by

$$N_X : \left(\begin{array}{c} \mathbf{L}^2(\hat{S}) \to \mathbf{L}^2(\hat{S}) \\ \mathbf{h} \mapsto \displaystyle\int_{\hat{S}} X_Y^s(x, y)\,\mathbf{h}(y)\,ds(y), \quad x \in \hat{S} \end{array} \right) \tag{20}$$

and

$$N_Y : \left(\begin{array}{c} \mathbf{L}^2(\hat{S}) \to \mathbf{L}^2(\hat{S}) \\ \mathbf{h} \mapsto \displaystyle\int_{\hat{S}} Y_X^s(x, y)\,\mathbf{h}(y)\,ds(y), \quad x \in \hat{S} \end{array} \right). \tag{21}$$

The Linear Sampling Method relies on the following theorem (see Theorem 3.6 in [1]). The proof of such theorem follows exactly the same lines as the proof of Theorem 2 in [34] by using the factorization of the operators N_X and N_Y which is derived and analyzed in [1].

Theorem 3. *Let N_X and N_Y be the near field operators defined by (20) and (21) and $\mathbf{p}$ be some unit vector in $\mathbb{R}^2$. Except maybe for a countable set of frequencies ω, the following statements hold:*

- *if $z \in D$, for all $\varepsilon > 0$ there exists some field $\mathbf{h}_\varepsilon(\cdot, z, \mathbf{p}) \in \mathbf{L}^2(\hat{S})$ such that*

$$\|N_X\mathbf{h}_\varepsilon - G_X^Y(\cdot, z)\,\mathbf{p}\|_{\mathbf{L}^2(\hat{S})} \le \varepsilon$$

  and some field $\mathbf{h}_\varepsilon(\cdot, z, \mathbf{p}) \in \mathbf{L}^2(\hat{S})$ such that

$$\|N_Y\mathbf{h}_\varepsilon - G_Y^X(\cdot, z)\,\mathbf{p}\|_{\mathbf{L}^2(\hat{S})} \le \varepsilon.$$

  In these two cases, for a given $\varepsilon > 0$,

$$\lim_{z \to \partial D} \|\mathbf{h}_\varepsilon(\cdot, z, \mathbf{p})\|_{\mathbf{L}^2(\hat{S})} = +\infty.$$

275   • *if $z \in \Omega_R = W_R \setminus \overline{D}$, for all field $\mathbf{h}_\varepsilon(\cdot, z, \mathbf{p}) \in \mathbf{L}^2(\hat{S})$ such that*

$$\|N_X \mathbf{h}_\varepsilon - G_X^Y(\cdot, z)\, \mathbf{p}\|_{\mathbf{L}^2(\hat{S})} \le \varepsilon \quad \text{or} \quad \|N_Y \mathbf{h}_\varepsilon - G_Y^X(\cdot, z)\, \mathbf{p}\|_{\mathbf{L}^2(\hat{S})} \le \varepsilon,$$

we have

$$\lim_{\varepsilon \to 0} \|\mathbf{h}_\varepsilon(\cdot, z, \mathbf{p})\|_{\mathbf{L}^2(\hat{S})} = +\infty.$$

Then a practical method to identify D from one of the operators N_X and N_Y and given a unit vector $\mathbf{p}$, consists for all z in some sampling grid, to solve in $\mathbf{L}^2(\hat{S})$ the equation

$$N_X \mathbf{h} = G_X^Y(\cdot, z)|_{\hat{S}}\, \mathbf{p} \tag{22}$$

280   or

$$N_Y \mathbf{h} = G_Y^X(\cdot, z)|_{\hat{S}}\, \mathbf{p} \tag{23}$$

and then to plot the function $\psi(z) = 1/\|\mathbf{h}(z)\|_{\mathbf{L}^2(\hat{S})}$, which from the above theorem turns out to be an indicator function of the defect.

4.2. The modal formulation

Now let us introduce the modal formulation of the LSM. To this end, let us
285   denote by $\mathbf{u}_n^{s\pm}$ the solution to problem (19) which corresponds to $\mathbf{f} = -\mathbf{u}_n^{\pm}|_{\partial D}$, where $\mathbf{u}_n^{\pm}$ are the guided modes given for $n \in \mathbb{N}$ by (10), and let us denote by $\mathbf{X}_n^{s\pm}$ the $\mathbf{X}$ extension of $\mathbf{u}_n^{s\pm}$. By our conjecture 2, we can decompose

$$\mathbf{X}_n^{s+}|_{S_{-R}} = -\sum_{m \in \mathbb{N}} S_{mn}^{+-} \boldsymbol{\mathcal{X}}_m, \quad \mathbf{X}_n^{s-}|_{S_{-R}} = -\sum_{m \in \mathbb{N}} S_{mn}^{--} \boldsymbol{\mathcal{X}}_m, \tag{24}$$

$$\mathbf{X}_n^{s+}|_{S_R} = \sum_{m \in \mathbb{N}} S_{mn}^{++} \boldsymbol{\mathcal{X}}_m, \quad \mathbf{X}_n^{s-}|_{S_R} = \sum_{m \in \mathbb{N}} S_{mn}^{-+} \boldsymbol{\mathcal{X}}_m. \tag{25}$$

Similarly, we set $\mathbf{h} = (\mathbf{h}_-, \mathbf{h}_+) \in \mathbf{L}^2(S_{-R}) \times \mathbf{L}^2(S_R)$ with

$$\mathbf{h}_- = -\sum_{n \in \mathbb{N}} h_n^- \boldsymbol{\mathcal{Y}}_n, \quad \mathbf{h}_+ = \sum_{n \in \mathbb{N}} h_n^+ \boldsymbol{\mathcal{Y}}_n.$$

290   It is proved in [1] that the equation (22) is equivalent to the infinite system

$$\begin{cases} \displaystyle\sum_{n \in \mathbb{N}} e^{i\beta_n R} \left(S_{mn}^{+-} h_n^- + S_{mn}^{--} h_n^+ \right) = e^{i\beta_m(R+z_3)} (\boldsymbol{\mathcal{X}}_m(z_1) \cdot \mathbf{p}) \\ \displaystyle\sum_{n \in \mathbb{N}} e^{i\beta_n R} \left(S_{mn}^{++} h_n^- + S_{mn}^{-+} h_n^+ \right) = -e^{i\beta_m(R-z_3)} (\boldsymbol{\mathcal{X}}_m(z_1) \cdot \mathbf{p}) \end{cases} \quad \forall m \in \mathbb{N}. \tag{26}$$

From (24) and (25), we can deduce that

$$\mathbf{Y}_n^{s+}|_{S_{-R}} = \sum_{m \in \mathbb{N}} S_{mn}^{+-} \boldsymbol{\mathcal{Y}}_m, \quad \mathbf{Y}_n^{s-}|_{S_{-R}} = \sum_{m \in \mathbb{N}} S_{mn}^{--} \boldsymbol{\mathcal{Y}}_m,$$

$$\mathbf{Y}_n^{s+}|_{S_R} = \sum_{m \in \mathbb{N}} S_{mn}^{++} \boldsymbol{\mathcal{Y}}_m, \quad \mathbf{Y}_n^{s-}|_{S_R} = \sum_{m \in \mathbb{N}} S_{mn}^{-+} \boldsymbol{\mathcal{Y}}_m,$$

11

so that by choosing now

$$\mathbf{h}_- = \sum_{n \in \mathbb{N}} h_n^- \boldsymbol{\mathcal{X}}_n, \quad \mathbf{h}_+ = \sum_{n \in \mathbb{N}} h_n^+ \boldsymbol{\mathcal{X}}_n,$$

we can prove similarly that the equation (23) is equivalent to the infinite system

$$\begin{cases} \displaystyle\sum_{n \in \mathbb{N}} e^{i\beta_n R} \left(S_{mn}^{+-} h_n^- + S_{mn}^{--} h_n^+ \right) = e^{i\beta_m(R+z_3)}(\boldsymbol{\mathcal{Y}}_m(z_1) \cdot \mathbf{p}) \\ \displaystyle\sum_{n \in \mathbb{N}} e^{i\beta_n R} \left(S_{mn}^{++} h_n^- + S_{mn}^{-+} h_n^+ \right) = e^{i\beta_m(R-z_3)}(\boldsymbol{\mathcal{Y}}_m(z_1) \cdot \mathbf{p}) \end{cases} \quad \forall m \in \mathbb{N}. \quad (27)$$

Like in acoustics, the above equivalence between the equation (22) (resp. the equation (23)) and the system (26) (resp. the system (27)) shows that it is equivalent:

- to know the **X** (resp. **Y**) extension of the scattered fields on $\hat{S}$ associated to all point sources $G_u^Y(\cdot, y)$ (resp. $G_u^X(\cdot, y)$) for $y \in \hat{S}$

- to know the projections on the $\boldsymbol{\mathcal{X}}_m$ (resp. $\boldsymbol{\mathcal{Y}}_m$) functions of the **X** (resp. **Y**) extension of the scattered fields on $\hat{S}$ associated to all the guided modes $\mathbf{u}_n^\pm$ for $m, n \in \mathbb{N}$.

However, the notion of polarization is new in elasticity compared to acoustics: while a single system is solved in acoustics (see [18]), four differents systems can be solved in 2D elasticity, because of the scalar products $(\boldsymbol{\mathcal{X}}_m \cdot \mathbf{p})$ and $(\boldsymbol{\mathcal{Y}}_m \cdot \mathbf{p})$ for $\mathbf{p} = (1, 0)$ and $\mathbf{p} = (0, 1)$. Since $\boldsymbol{\mathcal{X}} = (t_1, u_3)^T$ and $\boldsymbol{\mathcal{Y}} = (u_1, t_3)^T$, we obtain four different polarizations : u_1, u_3, t_1 and t_3.

Remark 4. *We have shown in [2] that when the defect is a Neumann crack instead of a void, it can be detected point by point by using polarizations t_1 and t_3. More precisely, the correct polarization is $t_1 \nu_1 - t_3 \nu_3$, where (ν_1, ν_3) is the local normal to the crack. Such normal can be obtained locally by an optimization process.*

4.3. The regularization

As proved in [1, 2], the near field operators N_X and N_Y are compact, so that the equations (22) and (23) are ill-posed. A convenient way to regularize the infinite systems (26) and (27) is then to restrict the indices m and n to the N first terms, where N is the finite number of propagating modes. Indeed, the evanescent and inhomogeneous modes do not contribute to the scattered field at a long distance from the defect, in particular on $\hat{S} = S_{-R} \cup S_R$ when R is large, only the propagating modes do. Let us specify such discretization for the system (27). We hence define the matrices and vectors

$$S^{-\pm} = (S_{mn}^{-\pm}), \quad S^{+\pm} = (S_{mn}^{+\pm}), \quad m, n = 0, \dots, N-1$$

$$H^\pm = (h_m^\pm), \quad F_{Y,p}^\pm = e^{i\beta_m(R \mp z_3)}(\boldsymbol{\mathcal{Y}}_m(z_1) \cdot \mathbf{p}), \quad m = 0, \dots, N-1.$$

We also introduce the $N \times N$ diagonal matrix K formed by the diagonal terms $e^{i\beta_n R}$, $n = 0, \ldots, N-1$, as well as the global matrices and vectors

$$\mathcal{S} = \left(\begin{array}{cc} S^{+-} & S^{--} \\ S^{++} & S^{-+} \end{array} \right), \; \mathcal{U} = \mathcal{S} \left(\begin{array}{cc} K & 0 \\ 0 & K \end{array} \right), \; H = \left(\begin{array}{c} H^- \\ H^+ \end{array} \right), \; \mathcal{F}_{Y,p} = \left(\begin{array}{c} F_{Y,p}^- \\ F_{Y,p}^+ \end{array} \right).$$

With those notations, the regularization applied to the infinite system (27) leads to the $2N \times 2N$ system

$$\mathcal{U}H = \mathcal{F}_{Y,p}. \tag{28}$$

We refer to the $2N \times 2N$ matrix $\mathcal{S}$ as the scattering matrix while we refer to the $2N \times 2N$ matrix $\mathcal{U}$ as the LSM matrix. In what follows it will be convenient to introduce the matrices $U^{-\pm} = S^{-\pm}K$, $U^{+\pm} = S^{+\pm}K$. Obviously, we obtain from (26) the same system as (28), except that the right-hand side $\mathcal{F}_{Y,p}$ is replaced by some vector $\mathcal{F}_{X,p}$. In view of the experimental setup of last section 7, it is important to address the back-scattering case, that is the data of the inverse problem are supported by S_{-R} instead of $\hat{S} = S_{-R} \cup S_R$. The inverse problem consists then in finding the obstacle D from the trace on S_{-R} of either $X_Y^s(\cdot, y)$ or $Y_X^s(\cdot, y)$, for all $y \in S_{-R}$. In the back-scattering situation, it is readily seen that the $2N \times 2N$ system (28) is replaced by the $N \times N$ system

$$U^{+-}H^- = F_{Y,p}^-. \tag{29}$$

Remark 5. *Here we highlight the fact that the system (28) is both a discretization and a regularization of the ill-posed problem (23). The discretization consists of a projection on the transverse modes $\boldsymbol{\mathcal{X}}_n$. The regularization consists in considering only the integers n associated with the propagating modes (this is justified in [18] in the acoustic case). This regularization seems relevant for at least two reasons. Firstly, it is based on a physical argument (the non-propagating modes vanish at long distance). Secondly, it leads to a very limited number of meaningful degrees of freedom. Such physical way to regularize the ill-posed problem would not be possible by handling the data directly in the time domain. In particular, this strongly motivates us to use the modal formulation and hence a multi-frequency approach rather than a time domain approach like in [25], as detailed in the next section.*

5. The case of surface data in the time domain

In this section, we explain how to exploit the modal formulation of the Linear Sampling Method exposed in section 4 to tackle the realistic NDT problem of section 2.

5.1. From time domain to frequency domain data

First of all, by taking the Fourier transform with respect to time t in the system (1), that is

$$\widehat{\mathbf{v}}(x, \omega) = \int_{\mathbb{R}} \mathbf{v}(x, t) e^{i\omega t} \, dt, \tag{30}$$

13

then for some fixed frequency $\omega > 0$ the solution $\mathbf{u} = \widehat{\mathbf{v}}(\cdot, \omega)$ satisfies the scattering problem in Ω_R:

$$
\begin{cases}
\operatorname{div}(\sigma(\mathbf{u})) + \rho\omega^2\mathbf{u} & = & 0 & \text{in } \Omega_R \\
\sigma(\mathbf{u})\,\boldsymbol{\nu} & = & \varphi_\omega\mathbf{e}_1 & \text{on } \Gamma_{d,R} \\
\sigma(\mathbf{u})\,\boldsymbol{\nu} & = & 0 & \text{on } \Gamma_{0,R} \\
\mathbf{u} & = & 0 & \text{on } \partial D \\
T_\pm\mathbf{Y} & = & \pm\mathbf{X} & \text{on } S_{\pm R},
\end{cases}
\tag{31}
$$

where $\Gamma_{d,R} = \Gamma_d \cap \Gamma_R$, $\Gamma_{0,R} = \Gamma_0 \cap \Gamma_R$ and $\varphi_\omega = \widehat{\chi}(\omega)\,\varphi$.

Remark 6. *It is fundamental to consider the exponential $e^{i\omega t}$ and not $e^{-i\omega t}$ in our definition (30) of the Fourier transform in order that $\mathbf{u}$ satisfies the radiation condition in problem (31). In the slightly simpler case of acoustics, this fact is fully justified in [29] with the help of the limiting absorption principle. Besides, the definition of (30) requires $\mathbf{v}$ to be sufficiently decreasing with respect to time t at infinity. This aspect is discussed in the numerical section. In the presence of experimental data, the Fourier transform is of course replaced by the discrete Fourier transform.*

For convenience, we also introduce the solution $\mathbf{u}^i$ to the system

$$
\begin{cases}
\operatorname{div}(\sigma(\mathbf{u}^i)) + \rho\omega^2\mathbf{u}^i & = & 0 & \text{in } W_R \\
\sigma(\mathbf{u}^i)\,\boldsymbol{\nu} & = & \varphi_\omega\mathbf{e}_1 & \text{on } \Gamma_{d,R} \\
\sigma(\mathbf{u}^i)\,\boldsymbol{\nu} & = & 0 & \text{on } \Gamma_{0,R} \\
T_\pm\mathbf{Y}^i & = & \pm\mathbf{X}^i & \text{on } S_{\pm R}.
\end{cases}
\tag{32}
$$

As a result, $\mathbf{u}$ is the total field while $\mathbf{u}^i$ is the incident field and $\mathbf{u}^s = \mathbf{u} - \mathbf{u}^i$ is the scattered one. Besides, the scattered field $\mathbf{u}^s$ is solution to problem (19) with $\mathbf{f} = -\mathbf{u}^i|_{\partial D}$. A convenient way to give an explicit expression of $\mathbf{u}^i$ is to use the fundamental solution of problem (32), which corresponds to the particular case when φ_ω is chosen as the Dirac distribution δ at point y_3. As proved in Appendix A, such fundamental solution coincides with $G_u^{t_1}$, which is obtained by selecting among the rows of matrix G given by (18) those which correspond to the components of $\mathbf{u}$ and by selecting the first column of G, that corresponds to the component t_1. The vector function G^{t_1} is hence given by

$$
\begin{pmatrix} G_X^{t_1} \\ G_Y^{t_1} \end{pmatrix} = -\sum_{n\in\mathbb{N}} \begin{pmatrix} s(x_3 - y_3)\boldsymbol{\mathcal{X}}_n(x_1) \\ \boldsymbol{\mathcal{Y}}_n(x_1) \end{pmatrix} \frac{u_1^n(d)}{2} e^{i\beta_n|x_3 - y_3|}.
$$

By convolution, it is readily seen that the incident field $\mathbf{u}^i$ in the extended variables $\mathbf{X}, \mathbf{Y}$ is expressed as

$$
\begin{pmatrix} \mathbf{X}^i \\ \mathbf{Y}^i \end{pmatrix} = -\sum_{n\in\mathbb{N}} \int_{\mathbb{R}} \begin{pmatrix} s(x_3 - y_3)\boldsymbol{\mathcal{X}}_n(x_1) \\ \boldsymbol{\mathcal{Y}}_n(x_1) \end{pmatrix} \frac{u_1^n(d)}{2} e^{i\beta_n|x_3 - y_3|}\varphi_\omega(y_3)\,dx_3. \tag{33}
$$

14

5.2. From surface to modal data

We will need the following lemma.

Lemma 7. *For $R' > R$ and $\mathbf{g} \in H^{\frac{1}{2}}(S_R) \times \tilde{H}^{-\frac{1}{2}}(S_R)$, the extension $\mathbf{Y}$ of the solution $\mathbf{u}$ to the problem*

$$
\begin{cases}
\mathrm{div}(\sigma(\mathbf{u})) + \rho\omega^2\mathbf{u} &= 0 & \text{in } S \times (R, R') \\
\sigma(\mathbf{u})\,\boldsymbol{\nu} &= 0 & \text{on } (\{x_1 = d\} \cup \{x_1 = 0\}) \times (R, R') \\
\mathbf{Y} &= \mathbf{g} & \text{on } S_R \\
T_+\mathbf{Y} &= \mathbf{X} & \text{on } S_{R'}
\end{cases}
\tag{34}
$$

is given by

$$
\mathbf{Y}(x) = \sum_{n \in \mathbb{N}} (\boldsymbol{\mathcal{X}}_n | \mathbf{g})_{S_R} e^{i\beta_n(x_3 - R)} \boldsymbol{\mathcal{Y}}_n(x_1). \tag{35}
$$

Symmetrically, the extension $\mathbf{Y}$ of the solution $\mathbf{u}$ to the problem

$$
\begin{cases}
\mathrm{div}(\sigma(\mathbf{u})) + \rho\omega^2\mathbf{u} &= 0 & \text{in } S \times (-R', -R) \\
\sigma(\mathbf{u})\,\boldsymbol{\nu} &= 0 & \text{on } (\{x_1 = d\} \cup \{x_1 = 0\}) \times (-R', -R) \\
\mathbf{Y} &= \mathbf{g} & \text{on } S_{-R} \\
T_-\mathbf{Y} &= -\mathbf{X} & \text{on } S_{-R'}
\end{cases}
\tag{36}
$$

is given by

$$
\mathbf{Y}(x) = \sum_{n \in \mathbb{N}} (\boldsymbol{\mathcal{X}}_n | \mathbf{g})_{S_{-R}} e^{-i\beta_n(x_3 + R)} \boldsymbol{\mathcal{Y}}_n(x_1). \tag{37}
$$

Proof. Let us begin with the first case (34). From Lemma 2.8 in [1], the solution to the first two common equations of systems (34) and (36) is given by

$$
\begin{pmatrix} \mathbf{X}(x) \\ \mathbf{Y}(x) \end{pmatrix} = \sum_{n \in \mathbb{N}} a_n^+ \begin{pmatrix} \mathbf{X}_n^+(x) \\ \mathbf{Y}_n^+(x) \end{pmatrix} + a_n^- \begin{pmatrix} \mathbf{X}_n^-(x) \\ \mathbf{Y}_n^-(x) \end{pmatrix}
$$

for some complex numbers a_n^+ and a_n^-. Given the expression (10) of the guided modes $\mathbf{X}_n^\pm, \mathbf{Y}_n^\pm$, we obtain in particular

$$
\mathbf{X}(x) = \sum_{n \in \mathbb{N}} (a_n^+ e^{i\beta_n x_3} - a_n^- e^{-i\beta_n x_3}) \boldsymbol{\mathcal{X}}_n(x_1)
$$

and

$$
\mathbf{Y}(x) = \sum_{n \in \mathbb{N}} (a_n^+ e^{i\beta_n x_3} + a_n^- e^{-i\beta_n x_3}) \boldsymbol{\mathcal{Y}}_n(x_1).
$$

From the definition (14) of the operator T, we have $T\boldsymbol{\mathcal{Y}}_n = \boldsymbol{\mathcal{X}}_n$ for all n, then the radiation condition on S'_R implies

$$
\sum_{n \in \mathbb{N}} (a_n^+ e^{i\beta_n R'} + a_n^- e^{-i\beta_n R'}) \boldsymbol{\mathcal{X}}_n(x_1) = \sum_{n \in \mathbb{N}} (a_n^+ e^{i\beta_n R'} - a_n^- e^{-i\beta_n R'}) \boldsymbol{\mathcal{X}}_n(x_1),
$$

that is $a_n^- = 0$ for all $n \in \mathbb{N}$. Lastly we use the boundary condition on S_R, that is

$$\mathbf{Y}(x) = \sum_{n \in \mathbb{N}} a_n^+ e^{i\beta_n R} \boldsymbol{\mathcal{Y}}_n(x_1) = \mathbf{g}(x),$$

which implies by using the biorthogonality relationship (11) that

$$a_n^+ e^{i\beta_n R} = (\boldsymbol{\mathcal{X}}_n | \mathbf{g})_{S_R}$$

for all n, and we end up with (35). Let us now consider the other case (36). The radiation condition on $S_{-R'}$ now gives

$$\sum_{n \in \mathbb{N}} (a_n^+ e^{-i\beta_n R'} + a_n^- e^{i\beta_n R'}) \boldsymbol{\mathcal{X}}_n(x_1) = -\sum_{n \in \mathbb{N}} (a_n^+ e^{-i\beta_n R'} - a_n^- e^{i\beta_n R'}) \boldsymbol{\mathcal{X}}_n(x_1),$$

that is $a_n^+ = 0$ for all $n \in \mathbb{N}$. The boundary condition on S_{-R} implies that

$$\mathbf{Y}(x) = \sum_{n \in \mathbb{N}} a_n^- e^{i\beta_n R} \boldsymbol{\mathcal{Y}}_n(x_1) = \mathbf{g}(x),$$

so that

$$a_n^- e^{i\beta_n R} = (\boldsymbol{\mathcal{X}}_n | \mathbf{g})_{S_{-R}}$$

for all n, and we end up with (37). $\qquad\square$

We have now to consider four configurations separately, depending on the fact that the source or the receiver is on the left or on the right of the defect. Let us first consider a left source located at point (d, y_3^{s-}) with $y_3^{s-} = -R - s\delta$, for $s = 0, \ldots, M-1$. From (33), the incident field is

$$\left(\begin{array}{c} \mathbf{X}^i(x) \\ \mathbf{Y}^i(x) \end{array} \right) = -\sum_{n \in \mathbb{N}} \left(\begin{array}{c} \boldsymbol{\mathcal{X}}_n(x_1) \\ \boldsymbol{\mathcal{Y}}_n(x_1) \end{array} \right) \frac{u_1^n(d)}{2} \int_{\mathbb{R}} e^{i\beta_n(x_3 - y_3)} \varphi_\omega(y_3) \, dy_3$$

$$= -\sum_{n \in \mathbb{N}} \left(\begin{array}{c} \mathbf{X}_n^+(x) \\ \mathbf{Y}_n^+(x) \end{array} \right) \frac{u_1^n(d)}{2} \int_{\mathbb{R}} e^{-i\beta_n y_3} \varphi_\omega(y_3) \, dy_3.$$

The corresponding scattered field is then

$$\left(\begin{array}{c} \mathbf{X}^s(x) \\ \mathbf{Y}^s(x) \end{array} \right) = -\sum_{n \in \mathbb{N}} \left(\begin{array}{c} \mathbf{X}_n^{s+}(x) \\ \mathbf{Y}_n^{s+}(x) \end{array} \right) \frac{u_1^n(d)}{2} \int_{\mathbb{R}} e^{-i\beta_n y_3} \varphi_\omega(y_3) \, dy_3,$$

where we recall that $\mathbf{X}_n^{s+}, \mathbf{Y}_n^{s+}$ are the $\mathbf{X}, \mathbf{Y}$ extensions of $\mathbf{u}_n^{s\pm}$, which is itself the solution to problem (19) associated with $\mathbf{f} = -\mathbf{u}_n^\pm|_{\partial D}$. Since $\varphi_\omega(y_3) = f_\omega(y_3 - y_3^{s-})$, where $f_\omega = \widehat{\chi}(\omega) f$, and taking into account the fact that f is an even function, we obtain

$$\mathbf{Y}^s(x) = -\sum_{n \in \mathbb{N}} \mathbf{Y}_n^{s+}(x) \frac{u_1^n(d)}{2} e^{i\beta_n(R+s\delta)} \int_{\mathbb{R}} e^{i\beta_n z} f_\omega(z) \, dz.$$

16

Let us now consider a reception point (d, x_3) located on the right of the waveguide. By using Lemma 7 in the case of (34) and given the definition of the scattering matrix S^{++}, we have that

$$\mathbf{Y}_n^{s+}(d, x_3) = \sum_{m \in \mathbb{N}} (\boldsymbol{\mathcal{X}}_m | \mathbf{Y}_n^{s+})_{S_R} e^{i\beta_m(x_3 - R)} \boldsymbol{\mathcal{Y}}_m(d) = \sum_{m \in \mathbb{N}} e^{i\beta_m(x_3 - R)} S_{mn}^{++} \boldsymbol{\mathcal{Y}}_m(d).$$

By plugging this identity in the expression of $\mathbf{Y}^s$, we obtain

$$\mathbf{Y}^s(d, x_3) = -\frac{\widehat{\chi}(\omega)}{2} \sum_{m,n \in \mathbb{N}} e^{i\beta_m(x_3 - R)} S_{mn}^{++} u_1^n(d) e^{i\beta_n(R + s\delta)} f_n \boldsymbol{\mathcal{Y}}_m(d),$$

where

$$f_n = \int_{\mathbb{R}} e^{i\beta_n z} f(z)\, dz. \tag{38}$$

In view of (3), the Fourier transform of the measurement at the receiver located at $x_3^{r+} = R + r\delta$, for $r = 0, \ldots, M - 1$, is given by

$$\widehat{\gamma}(x_3^{r+}, \omega) = \int_{\mathbb{R}} g(x_3 - x_3^{r+}) \mathsf{u}_1^s(d, x_3)\, dx_3,$$

that is

$$\widehat{\gamma}(x_3^{r+}, \omega) = -\frac{\widehat{\chi}(\omega)}{2} \sum_{m,n \in \mathbb{N}} e^{i\beta_m r\delta} g_m u_1^m(d) S_{mn}^{++} e^{i\beta_n R} u_1^n(d) f_n e^{i\beta_n s\delta},$$

where

$$g_m = \int_{\mathbb{R}} e^{i\beta_m z} g(z)\, dz. \tag{39}$$

By restricting the two sums to the first N terms, where N is the number of propagating modes, we obtain that for $r, s = 0, \ldots, M - 1$, the measurement M_{rs}^{++} obtained at point $x_3^{r+} = R + r\delta$ for a source located at $y_3^{s-} = -R - s\delta$ is approximately given by

$$M_{rs}^{++} = -\frac{\widehat{\chi}(\omega)}{2} \sum_{m,n=0}^{N-1} e^{ir\beta_m \delta} g_m u_1^m(d) U_{mn}^{++} u_1^n(d) f_n e^{i\beta_n s\delta},$$

where we have used the fact that $U^{++} = S^{++} K$. Using matrices, we obtain that

$$M^{++} = -\frac{\widehat{\chi}(\omega)}{2} R U^{++} E^T, \tag{40}$$

where

$$R = V F_g T, \quad E = V F_f T \tag{41}$$

and

- F_f and F_g are the $N \times N$ diagonal matrices formed by the diagonal terms f_n and g_n, respectively,

17

- T is the $N \times N$ diagonal matrix formed by the diagonal terms $u_1^n(d)$,

- V is the $M \times N$ Vandermonde matrix given by

$$V_{mn} = e^{im\beta_n\delta}, \quad m = 0, \ldots, M-1, \quad n = 0, \ldots, N-1. \qquad (42)$$

In what follows, the matrices F_f and F_g will be called the source shape and receiver shape matrices, the matrix T will be called the matrix of modes, while the matrices R and E will be called the reception and emission matrices.

Let us now consider a reception point (d, x_3) located on the left of the waveguide. By using Lemma 7 in the case of (36) and by the definition of the scattering matrix S^{+-}, we have that

$$\mathbf{Y}_n^{s+}(d, x_3) = \sum_{m\in\mathbb{N}} (\boldsymbol{\mathcal{X}}_m | \mathbf{Y}_n^{s+})_{S_{-R}} e^{-i\beta_m(x_3+R)} \boldsymbol{\mathcal{Y}}_m(d) = \sum_{m\in\mathbb{N}} e^{-i\beta_m(x_3+R)} S_{mn}^{+-} \boldsymbol{\mathcal{Y}}_m(d).$$

For a source located at point (d, y_3^{s-}), we hence obtain

$$\mathbf{Y}^s(d, x_3) = -\frac{\widehat{\chi}(\omega)}{2} \sum_{m,n\in\mathbb{N}} e^{-i\beta_m(x_3+R)} S_{mn}^{+-} e^{i\beta_n R} u_1^n(d) e^{i\beta_n s\delta} f_n \boldsymbol{\mathcal{Y}}_m(d).$$

The Fourier transform of the measurement at the receiver located at $x_3^{r-} = -R - r\delta$, for $r = 0, \ldots, M-1$, is given by

$$\widehat{\gamma}(x_3^{r-}, \omega) = -\frac{\widehat{\chi}(\omega)}{2} \sum_{m,n\in\mathbb{N}} e^{i\beta_m r\delta} g_m u_1^m(d) S_{mn}^{+-} e^{i\beta_n R} u_1^n(d) f_n e^{i\beta_n s\delta},$$

so that for $r, s = 0, \ldots, M-1$, the measurement M_{rs}^{+-} for a receiver located at $x_3^{r-} = -R - r\delta$ and for a source located at $x_3^{s-} = -R - s\delta$ is approximated by

$$M_{rs}^{+-} = -\frac{\widehat{\chi}(\omega)}{2} \sum_{m,n=0}^{N-1} e^{ir\beta_m\delta} g_m u_1^m(d) U_{mn}^{+-} u_1^n(d) f_n e^{i\beta_n s\delta},$$

that is

$$M^{+-} = -\frac{\widehat{\chi}(\omega)}{2} R U^{+-} E^T. \qquad (43)$$

Let us now consider a right source located at point (d, y_3^{s+}) with $y_3^{s+} = R + s\delta$, for $s = 0, \ldots, M-1$. From (33), the incident field is

$$\begin{pmatrix} \mathbf{X}^i(x) \\ \mathbf{Y}^i(x) \end{pmatrix} = -\sum_{n\in\mathbb{N}} \begin{pmatrix} -\boldsymbol{\mathcal{X}}_n(x_1) \\ \boldsymbol{\mathcal{Y}}_n(x_1) \end{pmatrix} \frac{u_1^n(d)}{2} \int_{\mathbb{R}} e^{-i\beta_n(x_3-y_3)} \varphi_\omega(y_3) \, dy_3$$

$$= -\sum_{n\in\mathbb{N}} \begin{pmatrix} \mathbf{X}_n^-(x) \\ \mathbf{Y}_n^-(x) \end{pmatrix} \frac{u_1^n(d)}{2} \int_{\mathbb{R}} e^{i\beta_n y_3} \varphi_\omega(y_3) \, dy_3$$

18

and the corresponding scattered field is then

$$\begin{pmatrix} \mathbf{X}^s(x) \\ \mathbf{Y}^s(x) \end{pmatrix} = -\sum_{n\in\mathbb{N}} \begin{pmatrix} \mathbf{X}_n^{s-}(x) \\ \mathbf{Y}_n^{s-}(x) \end{pmatrix} \frac{u_1^n(d)}{2} \int_{\mathbb{R}} e^{i\beta_n y_3} \varphi_\omega(y_3) \, dy_3.$$

By proceeding as previously, for $r, s = 0, \ldots, M-1$, the measurement M_{rs}^{-+} for a receiver located at $x_3^{r+} = R + r\delta$ and for a source located at $y_3^{s+} = R + s\delta$ is approximated by M_{rs}^{-+} such that

$$M^{-+} = -\frac{\widehat{\chi}(\omega)}{2} R U^{-+} E^T, \tag{44}$$

while the measurement M_{rs}^{--} for a receiver located at $x_3^{r-} = -R - r\delta$ and for a source located at $y_3^{s+} = R + s\delta$ is approximated by M_{rs}^{--} such that

$$M^{--} = -\frac{\widehat{\chi}(\omega)}{2} R U^{--} E^T. \tag{45}$$

Gathering all the previous contributions (40), (43), (44) and (45), we end up with

$$\mathcal{M} = -\frac{\hat{\chi}(\omega)}{2} \mathcal{R} \mathcal{U} \mathcal{E}^T, \tag{46}$$

where

$$\mathcal{M} = \begin{pmatrix} M^{+-} & M^{--} \\ M^{++} & M^{-+} \end{pmatrix}, \quad \mathcal{R} = \begin{pmatrix} R & 0 \\ 0 & R \end{pmatrix}, \quad \mathcal{E} = \begin{pmatrix} E & 0 \\ 0 & E \end{pmatrix}.$$

We hence conclude that for a given frequency, we can compute the LSM matrix $\mathcal{U}$ from the measurement matrix $\mathcal{M}$ by inverting the reception and emission matrices $\mathcal{R}$ and $\mathcal{E}$. In the case of back-scattering, the system to invert is reduced to (43).

5.3. The general strategy

The global strategy to solve the inverse problem in the full-scattering situation consists in the following steps:

1. Compute or measure the transverse component of the scattered field $\mathbf{v}^s$ in the time domain at all receivers $x_r^\pm$ for all sources $x_s^\pm$ for $r, s = 0, \ldots, M-1$.
2. Form the measurement matrix $\mathcal{M}(\omega)$ for all frequencies ω.
3. Invert the system (46) to obtain the LSM Matrix $\mathcal{U}(\omega)$ for all ω.
4. For all $z \in G$, where G is a sampling grid, compute the indicator function $\psi(z, \omega)$ by inverting the system (28).
5. Compute a global indicator function Ψ of the defect as

$$\Psi(z) = \left(\int_{\omega_-}^{\omega_+} \frac{\max_{z'\in G} |\psi(z', \omega)|^2}{|\psi(z, \omega)|^2} \, d\omega \right)^{-1/2}, \tag{47}$$

for some lower and upper bounds ω_- and ω_+.

19

In the back-scattering situation, we recall that the receivers and the sources are limited to x_r^- and x_s^- for $r, s = 0, \ldots, M-1$, the measurement matrix reduces to $M^{+-}(\omega)$, the LSM matrix reduces to $U^{+-}(\omega)$ and is obtained by inverting the system (43), lastly the LSM system to invert for all point z reduces to (29). We also recall that the indicator functions Ψ and $\psi(\cdot, \omega)$ are implicitly parametrized by one of the four polarizations u_1, u_3, t_1 and t_3. The definition of the global indicator function Ψ given by (47) corresponds to a "serial" combination. Such choice is discussed and justified in [26].

Remark 8. *We point out that in general, the system (28) should be solved in the Tikhonov sense (like in [35]), since the underlying operator to invert is compact. But in our case, since the system (28) is already regularized (see Remark 5) and small, an additional regularization is not necessary when the amplitude of noise is reasonable.*

5.4. On the inversion of the emission and reception matrices

A key point of our method is the computation of the LSM matrix $\mathcal{U}$ from the measurement matrix $\mathcal{M}$ given by (46), which amounts to inverting the reception and emission matrices R and E. Given their definition (41), we are led to check the invertibility of the source and receiver shape matrices F_f, F_g, the matrix of modes T and the Vandermonde matrix V.

5.4.1. The source/receiver shape matrices

Since the two matrices have the same form, we concentrate on the source shape matrix F_f, the diagonal term f_n of which is given by (38). We choose f such that none of the f_n vanishes for $n = 0, \ldots, N-1$. In particular, if f coincides with the Dirac function, F_f is the identity matrix. We expect that, if the function f is not "too far" from the Dirac, for example a hat function with a small support and a high amplitude, then F_f will be invertible and well conditioned.

5.4.2. The matrix of modes

The matrix of modes T is also diagonal, the diagonal term being given by $u_1^n(d)$ for $n = 0, \ldots, N-1$, where $u_1^n(d)$ is the transverse component of the nth mode given by (10) on the upper boundary of the waveguide. The matrix T is invertible if and only if none of the $u_1^n(d)$ vanishes for $n = 0, \ldots, N-1$. It happens that there are some exceptional values of ω such that one of the $u_1^n(d)$ vanishes. To be more specific, we prove the following theorem in appendix B, where the notion of symmetric/antisymmetric mode is also defined.

Theorem 9. *Let us assume that $\lambda > 0$. The matrix T is not invertible if and only if for some propagating mode $(\beta_n, \boldsymbol{\mathcal{X}}_n, \boldsymbol{\mathcal{Y}}_n)$, $n = 0, \ldots, N-1$, there exists $(p, q) \in \mathbb{N}^2$ such that p and q are either both odd or both even, with*

$$\beta_n^2 = \omega^2 \frac{\rho}{\mu} - \left(\frac{p\pi - 2\kappa_n}{d} \right)^2 = \omega^2 \frac{\rho}{\lambda + 2\mu} - \left(\frac{q\pi - 2\kappa_n}{d} \right)^2,$$

where $\kappa_n = 0$ if the mode is symmetric and $\kappa_n = \pi/2$ if it is antisymmetric.

20

We also prove in appendix B that for such mode, the corresponding β_n is associated with both a symmetric and an antisymmetric mode. From a geometric point of view, this means that if we plot the dispersion curves associated with all the propagating guided modes in the plane (ω, β), the cases when T is not invertible are those which correspond to the intersection of four curves: a curve associated with a symmetric mode, a curve associated with an antisymmetric mode and two curves of equations given by

$$\beta^2 = \omega^2 \frac{\rho}{\mu} - \left(\frac{\pi m}{d}\right)^2 \tag{48}$$

and

$$\beta^2 = \omega^2 \frac{\rho}{\lambda + 2\mu} - \left(\frac{\pi n}{d}\right)^2, \tag{49}$$

for $m, n \in \mathbb{N}$, respectively. In the figure 2, above is represented the condition number of the matrix T as a function of the frequency ω, while below are represented the dispersion curves in the coordinates (ω, β), as well as the curves (48) and (49). Since T is a diagonal matrix, the condition number is the ratio between the largest diagonal term and the lowest one with respect to the complex norm. The parameters d, ρ, λ and μ are those which are chosen in the numerical section. We observe that the peaks in the condition number of T coincide with the intersections of the four curves mentioned above.
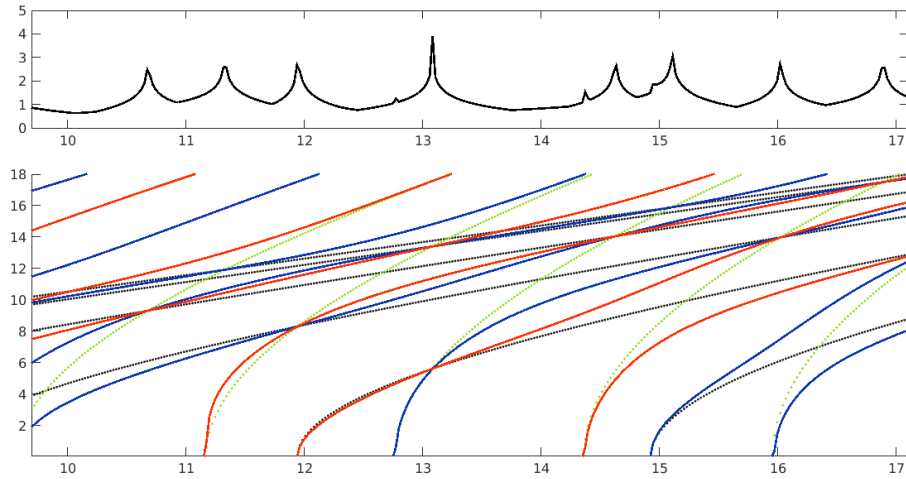

Figure 2: Above : logarithm of the condition number of the matrix T as a function of ω. Below : dispersion curves for symmetric modes (blue) and for antisymmetric modes (red), (48)-type of curve (dashed green), (49)-type of curve (dashed black).

5.4.3. The Vandermonde matrix

The invertibility and the conditioning of the rectangular Vandermonde matrix V given by (42) have already been studied in the acoustic case in [26].

21

However, the elastic case is more complicated since the β_n are not known analytically, contrary to the acoustic case. The matrix V depends only on the β_n, on the number M of sources and receivers and on the smallest distance δ between two sources or two receivers. It is recalled in the appendix A of [26] that for a Vandermonde matrix with entries on the unit circle, that is

$$V_{mn} = e^{2\pi i\, m f_n}, \quad m = 0, \ldots, M-1, \quad n = 0, \ldots, N-1,$$

for real numbers f_n and $M \geq N$, the matrix V^*V is invertible if and only if for all $n' \neq n$, $f_{n'} - f_n$ is not an integer. Here

$$f_n = \frac{\beta_n \delta}{2\pi}, \quad n = 0, \ldots, N-1.$$

An important issue, which can be seen on the dispersion curves, is that we may have $\beta_n(\omega) = \beta_{n'}(\omega)$ for $n \neq n'$ for some exceptional values of ω, that is multiple eigenvalues. The matrix V^*V is not invertible in that case. We hence assume from now on that ω is such that all the β_n are different, which in particular implies that the matrix of modes T is invertible. Since the β_n are ordered decreasingly, the invertibility of V^*V is achieved if the distance δ satisfies

$$\delta < \frac{2\pi}{\beta_0 - \beta_{N-1}}. \tag{50}$$

Let us consider now the condition number $\kappa(V)$ of V, which is defined by

$$\kappa(V) = \sqrt{\frac{\sigma_{\max}}{\sigma_{\min}}},$$

where $\sigma_{\max}$ and $\sigma_{\min}$ are the largest and smallest eigenvalues of V^*V, respectively. Let us introduce the wrap-around distance on the unit interval, that is

$$d_w(f, g) = \inf_{q \in \mathbb{Z}} |f - g + q|$$

as well as the minimal separation between the f_n as

$$\Delta = \min_{\substack{n,n'=0,\ldots,N-1 \\ n \neq n'}} d_w(f_n, f_{n'}). \tag{51}$$

The following theorem is proved in [36, 26].

Theorem 10. *If the minimal separation Δ defined by (51) satisfies $M > 1/\Delta + 1$, then*

$$\kappa(V) \leq \sqrt{\frac{M + 1/\Delta - 1}{M - 1/\Delta - 1}}.$$

Such theorem shows that $\kappa(V)$ is decreasing with respect to M and with respect to Δ. It is then tempting to use as many sources and receivers as possible. Maximizing Δ with respect to δ is desirable but contrary to the acoustic

case, it is rather difficult in elasticity due to the fact that the β_n are not known analytically. In the case when all the β_n are positive, which means that there are no inverse modes (the phase velocity and the group velocity have the same sign), we simply choose

$$\delta = \lambda_0 := \frac{2\pi}{\beta_0}, \tag{52}$$

which fulfills (50). In the acoustic case, it was proved in [26] that such choice of δ was the optimal one. In the figure 3, we have represented the condition number of the Vandermonde matrix V as a function of δ/λ_0, for $P = 12$ and for increasing values of M, that is $M = P$, $M = 2P$, $M = 4P$ and $M = 8P$. Such figure confirms that choosing δ as in (52) ensures the invertibility of V^*V and is a relevant value (the peaks correspond to the non-invertibility cases). It also confirms that the condition number improves when M increases.
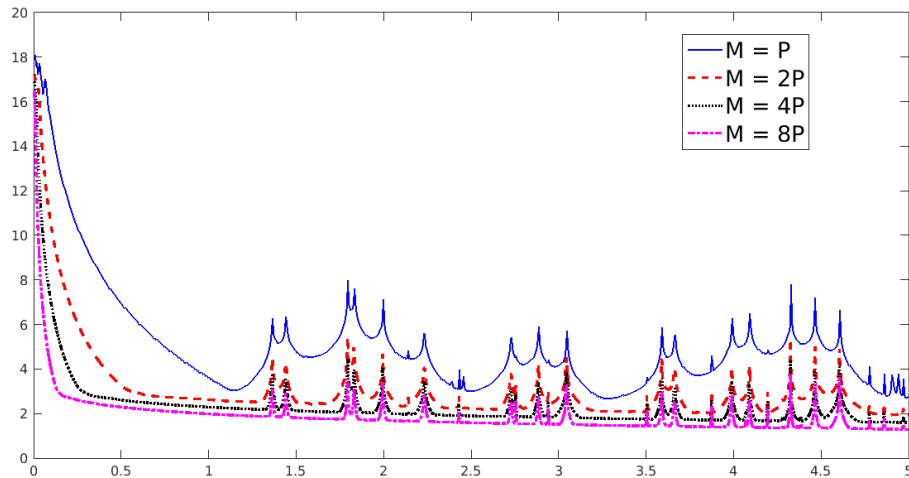

Figure 3: Logarithm of the condition number of the matrix V as a function of δ/λ_0, for $M = P$, $M = 2P$, $M = 4P$ and $M = 8P$.

6. Numerical results

In this section we test the strategy detailed in section 5.3 with the help of numerical experiments, not only for rigid obstacles, but also for voids and cracks. The height of the waveguide is $d = 1\,\mathrm{mm}$ and the selected material constants are

$$\lambda = 121\,\mathrm{GPa}, \quad \mu = 80\,\mathrm{GPa}, \quad \rho = 7900\,\mathrm{kg} \cdot \mathrm{m}^{-3}.$$

The artificial data are obtained by solving the forward problems (1) in the time domain. To this aim we use the code Echo, which is developed at CEA-List [37]. It relies on a spectral finite element method in space (with domain decomposition), a leap-frog scheme in time and Perfectly Matched Layers to bound

23

the domain. We also need the computation of the guided modes $(\beta_n, \boldsymbol{\mathcal{X}}_n, \boldsymbol{\mathcal{Y}}_n)$, which is based on the SAFE method [33, 38], which allows us to solve a generalized eigenvalue problem with the help of a finite element method. The function f in (2) is chosen as

$$f(x_3) = \frac{10}{d} \max\left(1 - \frac{10|x_3|}{d}, 0\right)$$

while the function χ is chosen as

$$\chi(t) = \sum_{n \in \mathcal{I}} \chi_n(t) = \sum_{n \in \mathcal{I}} [\sin(a_n t) \exp(-b_n(t - c_n)^2)]', \qquad (53)$$

with $\mathcal{I} \subset \mathbb{N}$. The shape of χ given by (53) is designed in such a way that the support of $\widehat{\chi}$ avoids all the cut-off frequencies ω_n, which are the frequencies such that there exists a guided mode with vanishing group velocity, that is $\partial \omega / \partial \beta_n = 0$. These are also the frequencies such that $(\boldsymbol{\mathcal{X}}_n | \boldsymbol{\mathcal{Y}}_n)_S = 0$ (see assumption 1). As detailed in [26], this enables us to obtain some scattered fields which decay rapidly with respect to time and then to reasonably bound the duration of the forward computations. But contrary to acoustics, these special frequencies ω_n have to be computed and are not equally distributed. Once they have been computed, the constants a_n, b_n and c_n are set to

$$\begin{cases} b_n = \dfrac{\pi^2}{200d^2}, \\[2mm] c_n = \dfrac{5}{\sqrt{2b_n}}, \\[2mm] \dfrac{a_n + \sqrt{a_n^2 + 16b_n}}{2} = \dfrac{1}{2}(\omega_n - \omega_{n-1}). \end{cases}$$

Moreover, we choose the set $\mathcal{I}$ of $n \in \mathbb{N}$ such that the support of χ_n is sufficiently small. In practice we have set $\mathcal{I} = \{8, 11, 14\}$. This implies that for all the frequencies which belong to the support of $\widehat{\chi}$, the corresponding number of propagating modes is 8, 11 or 14. The frequencies ω_- and ω_+ in (47) are the lower and upper bounds of the support of $\widehat{\chi}$, that is $\omega_- = \omega_7$ and $\omega_+ = \omega_{14}$. The function g in (3) is simply chosen as the Dirac distribution, which corresponds to a pointwise measurement. The number of sources/receivers on each side of the waveguide is $M = 42$ while the x_3 coordinate of the closest sensor is $R = 1$ and the distance δ between two sources/receivers is given by (52), with β_0 associated with the largest frequency ω, that is ω_+. The parameters M, R and δ governing the location of sources/receivers (see (4)) are then determined. The sampling grid G consists of the subpart of the waveguide delimited by $x_3 = -R$ and $x_3 = R$. In figure 4 we present some identifications results of an obstacle characterized by a Dirichlet boundary condition and formed by a square or two rectangles, either in the full-scattering situation or the back-scattering situation, with polarization u_1. We observe that the Dirichlet defects are well retrieved, in particular in the full-scattering situation, as expected. In figure 5 we present
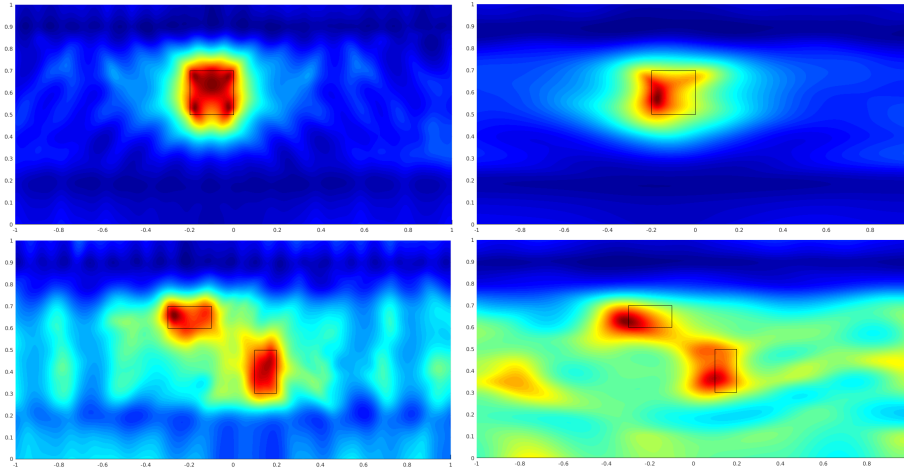
24

Figure 4: Obstacle with Dirichlet boundary condition. Top: one square. Bottom: two rectangles. Left: full-scattering situation. Right: back-scattering situation.

the same results for a square characterized by a Neumann boundary condition, in the full-scattering situation, and with two kinds of polarizations: t_1 and t_3. We observe that voids are not as well retrieve as Dirichlet defects, which is
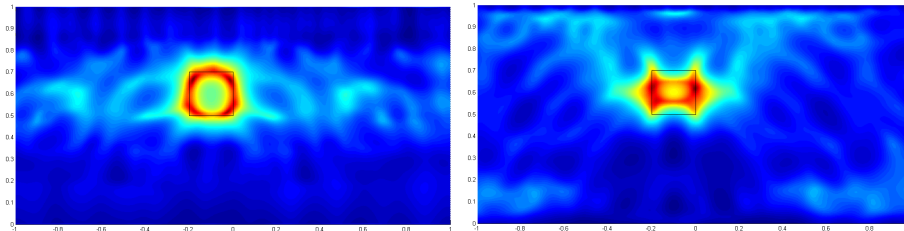

Figure 5: Obstacle with Neumann boundary condition in the full-scattering situation. Left: polarization t_1. Right: polarization t_3.

usual in sampling methods. Lastly, in figure 6 we present the same results for two straight cracks, in the full-scattering situation, and with polarizations t_1 and t_3. Those results are consistent with Remark 4: in the case of cracks, the polarization has to be in accordance with the local normal to the crack. The crack on the left is better retrieved with polarization t_1 while the crack on the right is better retrieved with polarization t_3. An optimization procedure to compute such local normal for curved cracks (not used here) is described in [2].
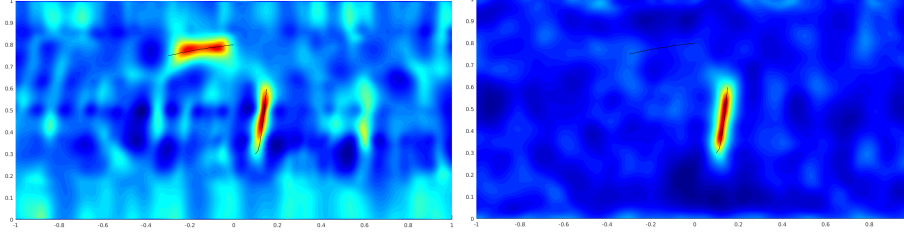
25

Figure 6: Case of two cracks in the full-scattering situation. Left: polarization t_1. Right: polarization t_3.

7. Experimental results

We complete this article with some experimental results on a steel plate of dimensions $12\,\text{mm} \times 110\,\text{mm} \times 500\,\text{mm}$ in the x_1, x_2 and x_3 directions, respectively. As shown in figure 7 (on the left), the plate is divided into 3 parts in the x_2 direction:

- a zone of width $50\,\text{mm}$ which doesn't contain any defect,

- a zone of width $10\,\text{mm}$ which contains a cylindrical notch, the section of which is a rectangle of dimension $0.25\,\text{mm}$ in the x_3 direction and $2\,\text{mm}$ in the direction x_1,

- a zone of width $50\,\text{mm}$ which contains a cylindrical hole, the section of which is a disc of diameter $2\,\text{mm}$.

The zone which is free of defect enables us to measure the incident field while the two others enable us to measure the total fields in the presence of the defect. The material constants of the plate are completely determined by measurements of the 3 following quantities: the density ρ, the celerity of P waves c_P and the celerity of S waves c_S, which in turn enable us to compute the Lamé constants λ and μ thanks to

$$c_P = \sqrt{\frac{\lambda + 2\mu}{\rho}}, \quad c_S = \sqrt{\frac{\mu}{\rho}}.$$

We have found

$$\rho = 7926\,\text{kg} \cdot \text{m}^{-3}, \quad c_P = 5897\,\text{m} \cdot \text{s}^{-1}, \quad c_S = 3225\,\text{m} \cdot \text{s}^{-1}.$$

A classical linear ultrasonic transducer array is used for the non-destructive inspection of the plate. More precisely, the mean frequency of that transducer is 2 Mhz and its bandwidth contains frequencies which correspond to 12 to 25 propagating modes. It consists of 128 elements of size $18\,\text{mm} \times 0.55\,\text{mm}$ in the x_2 and x_3 directions, respectively, the distance between two elements being $0.25\,\text{mm}$, which implies that the distance between two sources/receivers (see (4)) is $\delta = 0.8\,\text{mm}$. As concerns the signal which is actually obtained with such

26

transducer, the time function χ in (1) can be measured directly, while the space functions in (2) and (3) are both approximated by

$$f(x_3) = g(x_3) = e^{-x_3^2/\sigma^2} \chi_{[-\ell/2,\ell/2]}(x_3),$$

where ℓ is the size of the element in the x_3 direction, $\chi_{[-\ell/2,\ell/2]}$ is the indicator function of the segment $[-\ell/2,\ell/2]$ and σ is calibrated from experimental observations. We have chosen $\ell/\sigma = 1.1$. Note that the value of that ratio is not that sensitive. In the following experiments, only the back-scattering situation is tested. A photograph of the experimental setup is shown in figure 7 (on the right). As explained in the paragraph 5.4.3, the Vandermonde matrix V, and
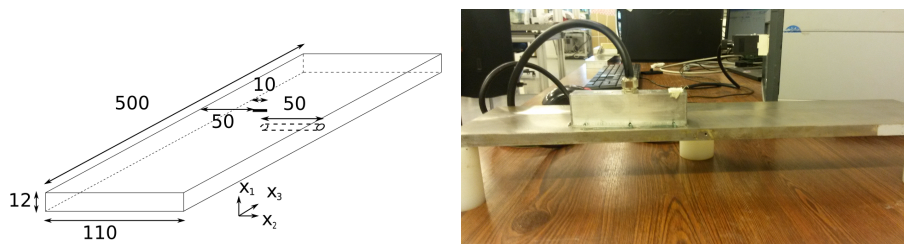

Figure 7: Left: scheme of the plate with defects. Right: experimental setup.

consequently the emission and reception matrices E and R, are not invertible when two distinct propagating modes are associated with the same wave number. It is well-known that at high frequencies ω the two eigenvalues $\beta_0(\omega)$ and $\beta_1(\omega)$ (which correspond to the first and second Lamb modes A_0 and S_0) actually become very close, which deteriorates the quality of the identification. This is why, if $|(\beta_0 - \beta_1)/\beta_0| < 10^{-5}$, only the first of these two modes is taken into account in the inversion procedure.

Remark 11. *Our specimen is far from being a true waveguide: its dimension in the x_3 direction is rather small, so that it can hardly be considered as a waveguide. In figure 8, we have represented the displacements measured at all receivers with respect to time for a given source (element number 128 of the transducer) and when the defect is the cylindrical hole. We can clearly distinguish 3 different waves: the wave emitted by the source (blue arrow), the wave scattered by the defect (green arrow) and the wave reflected by the edge of the plate (red arrow). We conclude that the total field is perturbed by some artifact due to the smallness of the plate length. Furthermore, the dimensions of the three zones of the specimen in the x_2 direction are rather small too, especially the cylindrical notch, so that it seems to contradict the 2D assumption. However, eventhough the assumptions of a 2D waveguide are violated somehow, we will see that the identification of defects is acceptable.*

In the figure 9, we can see the identification results obtained by our inversion procedure described in paragraph 5.3 (back-scattering case) from experimental data when the defect is the cylindrical hole. The chosen polarization is t_3. The
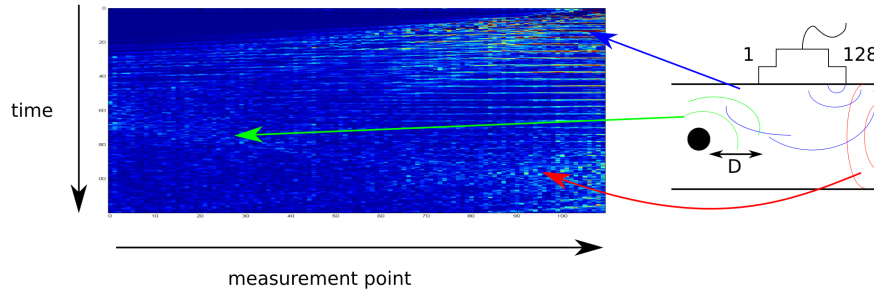
27

Figure 8: How the edge of the plate perturbs the measurements.

different pictures correspond to different distances D between the transducer and the defect. More precisely, the element number 1 of the transducer is exactly located on the left edge of the picture and is fixed (the element number 128 is outside the picture), so that the defect is moving to the right of the picture when the distance D increases. In the figure 10, the same identification results are shown when the defect is the cylindrical notch, again with polarization t_3.

In all cases, the defect is identified. But we observe that the smaller is the
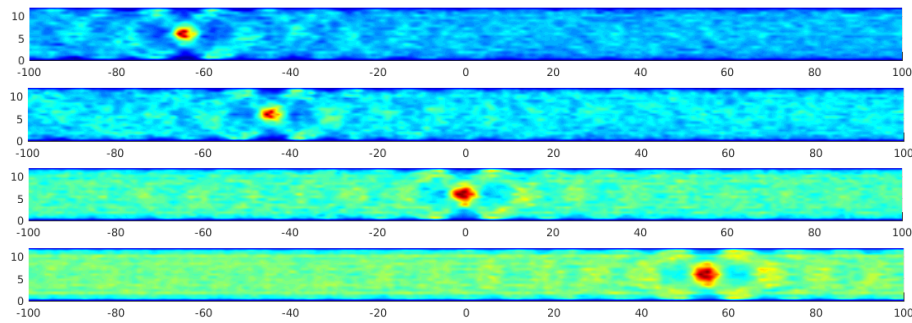
Figure 9: Identification of the cylindrical hole for $D = 35\,\mathrm{mm}$, $D = 55\,\mathrm{mm}$, $D = 95\,\mathrm{mm}$ and $D = 150\,\mathrm{mm}$.
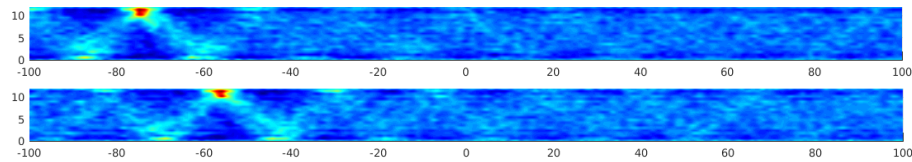
Figure 10: Identification of the cylindrical notch for $D = 25\,\mathrm{mm}$ and $D = 45\,\mathrm{mm}$.

distance between the transducer and the defect, the better is the resolution, which can be explained by some attenuation that is not taken into account

28

in our model. In the last figure 11, we show an identification result for the cylindrical hole with the help of another transducer of lower mean frequency 1 MHz, that is its bandwidth contains frequencies which correspond to 8 to 15 propagating modes. In addition, this transducer has 64 elements, the size of each element is $20\,\mathrm{mm} \times 0.9\,\mathrm{mm}$ in the x_2 and x_3 directions, respectively, the distance between two elements being $0.5\,\mathrm{mm}$, which implies that the distance between two sources/receivers in (4) is $\delta = 1.4\,\mathrm{mm}$. We expect some degradation in the quality of the identification, because the support of the functions f and g is bigger and above all the frequencies are lower, which is what we observe for two different distances D.
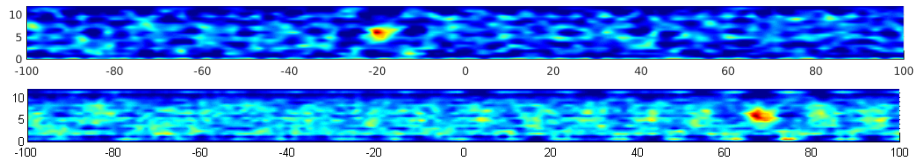

Figure 11: Identification of the cylindrical hole with a transducer of lower mean frequency for $D = 80\,\mathrm{mm}$ and $D = 170\,\mathrm{mm}$.

Remark 12. *The data used in our numerical validations were noise free. The influence of noise has already been studied in [26] in the acoustic case for numerical data and is actually the same in the elastic case. When experimental data are used, the presence of a small noise is inherent to the measurements, but we have seen that the reconstructions remain of good quality in that case.*

8. Conclusion

To conclude, the numerical and experimental identification results that we obtained in the present study enable us to be confident in the feasibility of the Linear Sampling Method to retrieve a wide class of defects in the context of ultrasonic NDT of waveguides. For simplicity, all the theory in our paper was presented in 2D, but it is also valuable in 3D, as shown in [1, 2] as well as in [29]. However, the design of experiments with 3D waveguides, which are tubes rather than plates, raise some new questions related to the geometry and the location of the transducers. Those questions are partially addressed in [29]. It would be certainly interesting to try the LSM for 3D geometries, both numerically and experimentally. More generally, from the experimental point of view, exploring other kinds of sensors and materials would be desirable in order to conclude on the future of sampling methods in the context of NDT.

Appendix A: The fundamental solution for a Dirac on the boundary

In this appendix, for $y = (d, y_3)$ we establish an expression of the solution $\mathcal{G}_u(\cdot, y)$ to the problem

$$\begin{cases} \operatorname{div}(\sigma(\mathcal{G}_u(\cdot, y)) + \rho\omega^2\mathcal{G}_u(\cdot, y) &= 0 & \text{in } \Omega_R \\ \sigma(\mathcal{G}_u(\cdot, y))\,\boldsymbol{\nu} &= \delta_{y_3}\mathbf{e}_1 & \text{on } \Gamma_{d,R} \\ \sigma(\mathcal{G}_u(\cdot, y))\,\boldsymbol{\nu} &= 0 & \text{on } \Gamma_{0,R} \\ T_{\pm}\mathcal{G}_Y(\cdot, y) &= \pm\mathcal{G}_X(\cdot, y) & \text{on } S_{\pm R}. \end{cases} \tag{54}$$

It is readily seen that the corresponding extended fundamental solution $\mathcal{G}(\cdot, y)$ satisfies the evolution equation

$$\begin{cases} \dfrac{\partial}{\partial x_3}\mathcal{G}(\cdot, y) = \begin{pmatrix} 0 & F_Y \\ F_X & 0 \end{pmatrix}\mathcal{G}(\cdot, y) & \text{in } W_R \\ \sigma_{11}(\mathcal{G}_Y(\cdot, y)) = \delta_{y_3}, \quad \mathsf{t}_1(\mathcal{G}_Y(\cdot, y)) = 0 & \text{on } \Gamma_{d,R} \\ \sigma_{11}(\mathcal{G}_Y(\cdot, y)) = 0, \quad \mathsf{t}_1(\mathcal{G}_Y(\cdot, y)) = 0 & \text{on } \Gamma_{0,R} \\ T_{\pm}\mathcal{G}_Y(\cdot, y) = \pm\mathcal{G}_X(\cdot, y) & \text{on } S_{\pm R}. \end{cases} \tag{55}$$

We will need the following lemma.

Lemma 13. *For sufficiently smooth* $\boldsymbol{\mathcal{X}} = (t_1, u_3)^T$, $\tilde{\boldsymbol{\mathcal{X}}} = (\tilde{t}_1, \tilde{u}_3)^T$, $\boldsymbol{\mathcal{Y}} = (u_1, t_3)^T$, $\tilde{\boldsymbol{\mathcal{Y}}} = (\tilde{u}_1, \tilde{t}_3)^T$, *we have*

$$(F_Y\boldsymbol{\mathcal{Y}}|\tilde{\boldsymbol{\mathcal{Y}}})_S - (\boldsymbol{\mathcal{Y}}|F_Y\tilde{\boldsymbol{\mathcal{Y}}})_S$$

$$= -\sigma_{11}(\boldsymbol{\mathcal{Y}})(d)\,\tilde{u}_1(d) + \sigma_{11}(\boldsymbol{\mathcal{Y}})(0)\,\tilde{u}_1(0) + \sigma_{11}(\tilde{\boldsymbol{\mathcal{Y}}})(d)\,u_1(d) - \sigma_{11}(\tilde{\boldsymbol{\mathcal{Y}}})(0)\,u_1(0)$$

and

$$(F_X\boldsymbol{\mathcal{X}}|\tilde{\boldsymbol{\mathcal{X}}})_S - (\boldsymbol{\mathcal{X}}|F_X\tilde{\boldsymbol{\mathcal{X}}})_S = t_1(d)\,\tilde{u}_3(d) - t_1(0)\,\tilde{u}_3(0) - \tilde{t}_1(d)\,u_3(d) + \tilde{t}_1(0)\,u_3(0).$$

Proof. From the definition of F_Y given by (7), we have

$$(F_Y\boldsymbol{\mathcal{Y}}|\tilde{\boldsymbol{\mathcal{Y}}})_S = -\int_0^d \left(\partial_{x_1}\sigma_{11}(\boldsymbol{\mathcal{Y}}) + \rho\,\omega^2 u_1\right)\tilde{u}_1\,ds - \int_0^d \left(\alpha\,\partial_{x_1}u_1 + \frac{\alpha}{\lambda}t_3\right)\tilde{t}_3\,ds.$$

By using the integration by parts formula, we have

$$\int_0^d \partial_{x_1}\sigma_{11}(\boldsymbol{\mathcal{Y}})\,\tilde{u}_1\,ds = -\int_0^d \sigma_{11}(\boldsymbol{\mathcal{Y}})\,\partial_{x_1}\tilde{u}_1\,ds + \sigma_{11}(\boldsymbol{\mathcal{Y}})(d)\,\tilde{u}_1(d) - \sigma_{11}(\boldsymbol{\mathcal{Y}})(0)\,\tilde{u}_1(0).$$

In addition, in view of (8), $\alpha\,\tilde{t}_3 = 2\mu(1 + \alpha)\partial_{x_1}\tilde{u}_1 - \sigma_{11}(\tilde{\boldsymbol{\mathcal{Y}}})$, we hence obtain

$$(F_Y\boldsymbol{\mathcal{Y}}|\tilde{\boldsymbol{\mathcal{Y}}})_S = -\sigma_{11}(\boldsymbol{\mathcal{Y}})(d)\,\tilde{u}_1(d) + \sigma_{11}(\boldsymbol{\mathcal{Y}})(0)\,\tilde{u}_1(0)$$

$$+ \int_0^d \left(\sigma_{11}(\boldsymbol{\mathcal{Y}})\partial_{x_1}\tilde{u}_1 + \sigma_{11}(\tilde{\boldsymbol{\mathcal{Y}}})\partial_{x_1}u_1 - 2\mu(1 + \alpha)\partial_{x_1}u_1\partial_{x_1}\tilde{u}_1 - \frac{\alpha}{\lambda}t_3\tilde{t}_3 - \rho\omega^2 u_1\tilde{u}_1\right)ds.$$

30

We notice that the integral term in the right-hand side is symmetric with respect to $\boldsymbol{\mathcal{Y}}$ and $\tilde{\boldsymbol{\mathcal{Y}}}$, so that we obtain the first equality. From the definition of F_X (see again (7)), we have

$$(F_X \boldsymbol{\mathcal{X}} | \tilde{\boldsymbol{\mathcal{X}}})_S = \int_0^d \left(\frac{t_1}{\mu} - \partial_{x_1} u_3 \right) \tilde{t}_1 \, ds + \int_0^d \left(\partial_{x_1} t_1 + \rho \omega^2 u_3 \right) \tilde{u}_3 \, ds,$$

which by using the integration by parts formula leads to

$$(F_X \boldsymbol{\mathcal{X}} | \tilde{\boldsymbol{\mathcal{X}}})_S = t_1(d) \tilde{u}_3(d) - t_1(0) \tilde{u}_3(0)$$

$$+ \int_0^d \left(-(\partial_{x_1} u_3 \, \tilde{t}_1 + \partial_{x_1} \tilde{u}_3 \, t_1) + \frac{1}{\mu} t_1 \tilde{t}_1 + \rho \omega^2 u_3 \tilde{u}_3 \right) \, ds.$$

Again the second equality stems from the symmetry of the integral term of the right-hand side with respect to $\boldsymbol{\mathcal{X}}$ and $\tilde{\boldsymbol{\mathcal{X}}}$. $\qquad \square$

In what follows, $\mathcal{D}(\mathbb{R})$ will denote the space of compactly supported and infinitely smooth functions on $\mathbb{R}$, while $\mathcal{D}'(\mathbb{R})$ will denote the space of distributions on $\mathbb{R}$. By multiplying the two equations of (55) by $\tilde{\mathbf{X}}_n(x_1, x_3) = \psi(x_3) \boldsymbol{\mathcal{X}}_n(x_1)$ and $\tilde{\mathbf{Y}}_n(x_1, x_3) = \psi(x_3) \boldsymbol{\mathcal{Y}}_n(x_1)$, where $\psi \in \mathcal{D}(\mathbb{R})$ with $\text{supp}(\psi) \subset (-R, R)$ and by integrating in W, we obtain

$$\begin{cases} \displaystyle \int_W \frac{\partial \mathcal{G}_X}{\partial x_3} \tilde{\mathbf{Y}}_n \, dx = \int_W (F_Y \mathcal{G}_Y) \tilde{\mathbf{Y}}_n \, dx \\ \displaystyle \int_W \frac{\partial \mathcal{G}_Y}{\partial x_3} \tilde{\mathbf{X}}_n \, dx = \int_W (F_X \mathcal{G}_X) \tilde{\mathbf{X}}_n \, dx, \end{cases}$$

that is

$$\begin{cases} \displaystyle \int_W \mathcal{G}_X \frac{\partial \tilde{\mathbf{Y}}_n}{\partial x_3} \, dx + \int_W (F_Y \mathcal{G}_Y) \tilde{\mathbf{Y}}_n \, dx = 0 \\ \displaystyle \int_W \mathcal{G}_Y \frac{\partial \tilde{\mathbf{X}}_n}{\partial x_3} \, dx + \int_W (F_X \mathcal{G}_X) \tilde{\mathbf{X}}_n \, dx = 0, \end{cases} \qquad (56)$$

By using the first equality of Lemma 13, we have

$$\int_W (F_Y \mathcal{G}_Y) \tilde{\mathbf{Y}}_n \, dx = \int_{\mathbb{R}} (F_Y \mathcal{G}_Y | \tilde{\mathbf{Y}}_n)_{S_{x_3}} \, dx_3 = \int_{\mathbb{R}} (\mathcal{G}_Y | F_Y \boldsymbol{\mathcal{Y}}_n)_{S_{x_3}} \psi(x_3) \, dx_3$$

$$- \int_{\Gamma_d} \sigma_{11}(\mathcal{G}_Y)(d, x_3) \, u_1^n(d) \psi(x_3) \, ds + \int_{\Gamma_0} \sigma_{11}(\mathcal{G}_Y)(0, x_3) \, u_1^n(0) \psi(x_3) \, ds$$

$$+ \int_{\Gamma_d} \sigma_{11}(\boldsymbol{\mathcal{Y}}_n)(d) \, \mathcal{G}_{u_1}(d, x_3) \psi(x_3) \, ds - \int_{\Gamma_0} \sigma_{11}(\boldsymbol{\mathcal{Y}}_n)(0) \, \mathcal{G}_{u_1}(0, x_3) \psi(x_3) \, ds.$$

The system (9) satisfied by the guided modes implies that $F_Y \boldsymbol{\mathcal{Y}}_n = i \beta_n \boldsymbol{\mathcal{X}}_n$ and $\sigma_{11}(\boldsymbol{\mathcal{Y}}_n)(d) = \sigma_{11}(\boldsymbol{\mathcal{Y}}_n)(0) = 0$. In addition, from the boundary conditions satisfied by $\sigma_{11}(\mathcal{G}_Y)$ on Γ_d and Γ_0 in (55), we end up with

$$\int_W (F_Y \mathcal{G}_Y) \tilde{\mathbf{Y}}_n \, dx = i \beta_n \int_{\mathbb{R}} (\mathcal{G}_Y | \boldsymbol{\mathcal{X}}_n)_{S_{x_3}} \psi(x_3) \, dx_3 - u_1^n(d) \psi(y_3). \qquad (57)$$

31

By using the second inequality of Lemma 13, we have

$$\int_W (F_X \mathcal{G}_X) \tilde{\mathbf{X}}_n \, dx = \int_{\mathbb{R}} (F_X \mathcal{G}_X | \tilde{\mathbf{X}}_n)_{S_{x_3}} \, dx_3 = \int_{\mathbb{R}} (\mathcal{G}_X | F_X \boldsymbol{\mathcal{X}}_n)_{S_{x_3}} \psi(x_3) \, dx_3$$

$$+ \int_{\Gamma_d} \mathcal{G}_{t_1}(d, x_3) \, u_3^n(d) \psi(x_3) \, ds - \int_{\Gamma_0} \mathcal{G}_{t_1}(0, x_3) \, u_3^n(0) \psi(x_3) \, ds$$

$$- \int_{\Gamma_d} t_1^n(d) \, \mathcal{G}_{u_3}(d, x_3) \psi(x_3) \, ds + \int_{\Gamma_0} t_1^n(0) \, \mathcal{G}_{u_3}(0, x_3) \psi(x_3) \, ds.$$

The system (9) satisfied by the guided modes implies that $F_X \boldsymbol{\mathcal{X}}_n = i\beta_n \boldsymbol{\mathcal{Y}}_n$ and $t_1^n(d) = t_1^n(0) = 0$. From the boundary conditions satisfied by $\mathcal{G}_{t_1}$ on Γ_d and Γ_0 in (55), we end up with

$$\int_W (F_X \mathcal{G}_X) \tilde{\mathbf{X}}_n \, dx = i\beta_n \int_{\mathbb{R}} (\mathcal{G}_X | \boldsymbol{\mathcal{Y}}_n)_{S_{x_3}} \psi(x_3) \, dx_3. \tag{58}$$

Gathering the equations (56), (57) and (58), we obtain

$$\begin{cases} \int_{\mathbb{R}} (\mathcal{G}_X | \boldsymbol{\mathcal{Y}}_n)_{S_{x_3}} \psi'(x_3) \, dx_3 + i\beta_n \int_{\mathbb{R}} (\mathcal{G}_Y | \boldsymbol{\mathcal{X}}_n)_{S_{x_3}} \psi(x_3) \, dx_3 = u_1^n(d) \psi(y_3) \\ \int_{\mathbb{R}} (\mathcal{G}_Y | \boldsymbol{\mathcal{X}}_n)_{S_{x_3}} \psi'(x_3) \, dx_3 + i\beta_n \int_{\mathbb{R}} (\mathcal{G}_X | \boldsymbol{\mathcal{Y}}_n)_{S_{x_3}} \psi(x_3) \, dx_3 = 0. \end{cases} \tag{59}$$

Plugging the decomposition

$$\begin{cases} \mathcal{G}_X(x_1, x_3) = \sum_{m \in \mathbb{N}} a_m(x_3) \boldsymbol{\mathcal{X}}_m(x_1) \\ \mathcal{G}_Y(x_1, x_3) = \sum_{m \in \mathbb{N}} b_m(x_3) \boldsymbol{\mathcal{Y}}_m(x_1) \end{cases}$$

in (59) and using the biothogonality condition $(\boldsymbol{\mathcal{X}}_n | \boldsymbol{\mathcal{Y}}_m)_S = \delta_{mn}$ for $m, n \in \mathbb{N}$, we obtain

$$\begin{cases} \int_{\mathbb{R}} a_n(x_3) \psi'(x_3) \, dx_3 + i\beta_n \int_{\mathbb{R}} b_n(x_3) \psi(x_3) \, dx_3 = u_1^n(d) \psi(y_3) \\ \int_{\mathbb{R}} b_n(x_3) \psi'(x_3) \, dx_3 + i\beta_n \int_{\mathbb{R}} a_n(x_3) \psi(x_3) \, dx_3 = 0, \end{cases}$$

which is equivalent, in the distributional sense in $\mathbb{R}$, to

$$\begin{cases} -a_n' + i\beta_n b_n = u_1^n(d) \delta_{y_3} \\ -b_n' + i\beta_n a_n = 0, \end{cases}$$

which in particular implies that

$$b_n'' + \beta_n^2 b_n = -i\beta_n u_1^n(d) \delta_{y_3}$$

The general solution to that equation in $\mathcal{D}'(\mathbb{R})$ is

$$b_n = -\frac{u_1^n(d)}{2} e^{i\beta_n |x_3 - y_3|} + A_n e^{i\beta_n x_3} + B_n e^{-i\beta_n x_3}.$$

32

Since the radiation condition implies that $A_n = B_n = 0$, we obtain that for all $n \in \mathbb{N}$,

$$a_n(x_3) = -s(x_3 - y_3)\frac{u_1^n(d)}{2}e^{i\beta_n|x_3-y_3|}, \quad b_n(x_3) = -\frac{u_1^n(d)}{2}e^{i\beta_n|x_3-y_3|}.$$

In conclusion, the expression of $\mathcal{G}(\cdot, y)$ for $y = (d, y_3)$ is

$$\begin{cases} \mathcal{G}_X(x, y) = -\sum_{n\in\mathbb{N}} s(x_3 - y_3)\frac{u_1^n(d)}{2}\boldsymbol{\mathcal{X}}_n(x_1)e^{i\beta_n|x_3-y_3|} \\ \mathcal{G}_Y(x, y) = -\sum_{n\in\mathbb{N}} \frac{u_1^n(d)}{2}\boldsymbol{\mathcal{Y}}_n(x_1)e^{i\beta_n|x_3-y_3|}. \end{cases}$$

We hence see that the vector function $\mathcal{G}(\cdot, y)$ for $y = (d, y_3)$ coincides with the first column $G^{t_1}(\cdot, y)$ of the fundamental solution $G(\cdot, y)$ given by (18).

Appendix B: The invertibility of the matrix of modes

This appendix provides a proof of Theorem 9, which is a necessary and sufficient condition to have $u_1^n(d) = 0$ for some $n = 0, \dots, N-1$. Let us recall that the behaviour of our 2D waveguide is governed by isotropic elasticity, the density is ρ and the Lamé constants are λ and μ. If β is associated with a propagating mode, then $-\beta$ is as well. Since $\beta \neq 0$, we can then assume without loss of generality that $\beta > 0$. From [39] (see also [33]), such β is a solution to the following dispersion relation:

$$\begin{aligned} &(\alpha_s^2 - \beta^2)^2 \cos\left(\frac{\alpha_p d}{2} + \kappa\right)\sin\left(\frac{\alpha_s d}{2} + \kappa\right) \\ &+4\beta^2\alpha_p\alpha_s \sin\left(\frac{\alpha_p d}{2} + \kappa\right)\cos\left(\frac{\alpha_s d}{2} + \kappa\right) = 0, \end{aligned} \tag{60}$$

with

$$\alpha_s^2 = k_s^2 - \beta^2, \quad \alpha_p^2 = k_p^2 - \beta^2, \quad k_s = \omega\sqrt{\frac{\rho}{\mu}}, \quad k_p = \omega\sqrt{\frac{\rho}{\lambda + 2\mu}}, \tag{61}$$

where $\kappa = 0$ or $\kappa = \pi/2$. The two components of the corresponding mode are given by

$$u_1(x_1) = -2A_p\alpha_p \sin\left(\alpha_p(x_1 - \frac{d}{2}) + \kappa\right) + 2A_s\beta \sin\left(\alpha_s(x_1 - \frac{d}{2}) + \kappa\right) \tag{62}$$

and

$$u_3(x_1) = 2A_p i\beta \cos\left(\alpha_p(x_1 - \frac{d}{2}) + \kappa\right) + 2A_s i\alpha_s \cos\left(\alpha_s(x_1 - \frac{d}{2}) + \kappa\right), \tag{63}$$

33

where the amplitudes A_p and A_s are obtained with the help of the free boundary condition, that is

$$\begin{cases} t \cos\left(\dfrac{\alpha_p d}{2} + \kappa\right) A_p - 2\beta\alpha_s \cos\left(\dfrac{\alpha_s d}{2} + \kappa\right) A_s = 0, \\[2mm] 2\beta\alpha_p \sin\left(\dfrac{\alpha_p d}{2} + \kappa\right) A_p + t \sin\left(\dfrac{\alpha_s d}{2} + \kappa\right) A_s = 0, \end{cases} \tag{64}$$

with $t = \alpha_s^2 - \beta^2$. The mode is said to be symmetric (resp. antisymmetric) if the component u_3 is symmetric (resp. antisymmetric) with respect to axis $x_1 = d/2$. The first case corresponds to $\kappa = 0$, while the second one corresponds to $\kappa = \pi/2$.

That the system (64) has a non trivial solution provides the dispersion relation (60). Under this condition, we can in general (provided the two terms in the right-hand side of (65) be not zero) choose the following amplitudes

$$\begin{cases} A_p = 2\beta\alpha_s \cos\left(\dfrac{\alpha_s d}{2} + \kappa\right) \\[2mm] A_s = t \cos\left(\dfrac{\alpha_p d}{2} + \kappa\right). \end{cases} \tag{65}$$

Plugging these amplitudes in (62), we obtain

$$\begin{aligned} u_1(d) = &-4\beta\alpha_s\alpha_p \sin\left(\frac{\alpha_p d}{2} + \kappa\right) \cos\left(\frac{\alpha_s d}{2} + \kappa\right) \\ &+2\beta t \sin\left(\frac{\alpha_s d}{2} + \kappa\right) \cos\left(\frac{\alpha_p d}{2} + \kappa\right). \end{aligned}$$

It follows from the dispersion relation (60) that

$$u_1(d) = \beta \sin\left(\frac{\alpha_s d}{2} + \kappa\right) \cos\left(\frac{\alpha_p d}{2} + \kappa\right) \left(\frac{(\alpha_s^2 - \beta^2)^2}{\beta^2} + 2t\right),$$

and lastly

$$u_1(d) = t \frac{k_s^2}{\beta} \sin\left(\frac{\alpha_s d}{2} + \kappa\right) \cos\left(\frac{\alpha_p d}{2} + \kappa\right). \tag{66}$$

Let us now study the different cases when $u_1(d) = 0$. From (66), this could occur in the 2 following cases.

1. The first case is $t = 0$. This implies that $\alpha_s^2 - \beta^2 = 0$, that is

$$\beta = \omega\sqrt{\frac{\rho}{2\mu}}.$$

Besides, from (60), the fact that $t = 0$ leads to

$$4\beta^2 \alpha_p \alpha_s \sin\left(\alpha_p \frac{d}{2} + \kappa\right) \cos\left(\alpha_s \frac{d}{2} + \kappa\right) = 0,$$

34

which from the fact that $\alpha_s \neq 0$ implies that

$$\alpha_p \sin\left(\alpha_p \frac{d}{2} + \kappa\right) \cos\left(\alpha_s \frac{d}{2} + \kappa\right) = 0.$$

Again we have to study 3 cases.

(a) The first sub-case is $\alpha_p = 0$. We have then $\beta = k_p = k_s/\sqrt{2}$, which in not possible since $\lambda > 0$.

(b) The second sub-case is $\sin(\alpha_p d/2 + \kappa) = 0$. Then there exists $p \in \mathbb{N}$ such that

$$\beta^2 = \omega^2 \frac{\rho}{\lambda + 2\mu} - \frac{4(p\pi - \kappa)^2}{d^2}.$$

This implies that $\beta = k_s/\sqrt{2} \leq k_p$, which is impossible since $\lambda > 0$

(c) The third sub-case is $\cos(\alpha_s d/2 + \kappa) = 0$. This case is also impossible. Indeed, if we substitute $t = 0$ and $\cos(\alpha_s d/2 + \kappa) = 0$ in the free boundary condition (64), we can take $A_p = 0$ and $A_s = 1$. It follows from (62) that

$$u_1(d) = 2\beta \sin\left(\frac{\alpha_s d}{2} + \kappa\right) \neq 0.$$

In conclusion, the case $t = 0$ is impossible.

2. The other case is $\sin(\alpha_s d/2 + \kappa) \cos(\alpha_p d/2 + \kappa) = 0$.
Then, the dispersion relation becomes

$$4\beta^2 \alpha_p \alpha_s \sin\left(\frac{\alpha_p d}{2} + \kappa\right) \cos\left(\frac{\alpha_s d}{2} + \kappa\right) = 0.$$

Since $\beta > 0$, we have again 3 cases to consider:

(a) The first sub-case is $\sin(\alpha_p d/2 + \kappa) \cos(\alpha_s d/2 + \kappa) = 0$. This identity, together with $\sin(\alpha_s d/2 + \kappa) \cos(\alpha_p d/2 + \kappa) = 0$, implies that either

$$\sin\left(\frac{\alpha_s d}{2} + \kappa\right) = \sin\left(\frac{\alpha_p d}{2} + \kappa\right) = 0$$

or

$$\cos\left(\frac{\alpha_s d}{2} + \kappa\right) = \cos\left(\frac{\alpha_p d}{2} + \kappa\right) = 0.$$

We obtain that there exists $(p, q) \in \mathbb{N}^2$, p and q being both odd or both even such that

$$\begin{cases} \beta^2 = \omega^2 \frac{\rho}{\mu} - \frac{(p\pi - 2\kappa)^2}{d^2}, \\ \beta^2 = \omega^2 \frac{\rho}{\lambda + 2\mu} - \frac{(q\pi - 2\kappa)^2}{d^2}. \end{cases} \tag{67}$$

(b) The second sub-case is $\alpha_p = 0$, that is

$$\beta = \omega \sqrt{\frac{\rho}{\lambda + 2\mu}}.$$

Besides, since $\sin(\alpha_s d/2 + \kappa)\cos(\alpha_p d/2 + \kappa) = 0$, either $\kappa = \pi/2$ or $\sin(\alpha_s d/2 + \kappa) = 0$. From (62), (63) and (65), we note that if $\kappa = \pi/2$, then $A_s = 0$ and therefore the two components of the displacement vanish, which we exclude. We hence infer that $\sin(\alpha_s d/2 + \kappa) = 0$ and $\kappa = 0$. That $\sin(\alpha_s d/2) = 0$ implies that there exists $m \in \mathbb{N}$ such that

$$\beta^2 = \omega^2 \frac{\rho}{\mu} - \left(\frac{2m\pi}{d}\right)^2.$$

We notice that such case is a particular case of (67), with $\kappa = 0$, $p = 2m$ and $q = 0$.

(c) The third sub-case is $\alpha_s = 0$, that is

$$\beta = \omega \sqrt{\frac{\rho}{\mu}}.$$

Besides, since $\sin(\alpha_s d/2 + \kappa)\cos(\alpha_p d/2 + \kappa) = 0$, either $\kappa = 0$ or $\cos(\alpha_p d/2 + \kappa) = 0$. From (62), (63) and (65), we note that if $\kappa = 0$, then $A_p = 0$ and therefore the two components of the displacement vanish, which we exclude. We hence have $\cos(\alpha_p d/2 + \kappa) = 0$ and $\kappa = \pi/2$, which implies there exists $m \in \mathbb{N}$ such that

$$\beta^2 = \omega^2 \frac{\rho}{\lambda + 2\mu} - \left(\frac{2m\pi}{d}\right)^2.$$

This never happens because $\beta = k_s \leq k_p$, which is impossible since $\lambda > 0$.

Conversely, the condition (67) implies that T is not invertible. This completes the proof of Theorem 9.

Remark 14. *From the above analysis, it happens that when the condition (67) is satisfied, except when $\kappa = 0$, p is even and $q = 0$, the corresponding β_n is both associated with a symmetric and an antisymmetric mode.*

References

[1] L. Bourgeois, F. Le Louer, E. Lunéville, On the use of Lamb modes in the linear sampling method for elastic waveguides, Inverse Problems 27 (5) (2011) 055001.
URL http://stacks.iop.org/0266-5611/27/i=5/a=055001

[2] L. Bourgeois, E. Lunéville, On the use of the linear sampling method to identify cracks in elastic waveguides, Inverse Problems 29 (2) (2013) 025017.
URL http://stacks.iop.org/0266-5611/29/i=2/a=025017

[3] P. Huthwaite, Evaluation of inversion approaches for guided wave thickness mapping, Proceedings of the Royal Society of London A: Mathematical, Physical and Engineering Sciences 470. `arXiv:http://rspa.royalsocietypublishing.org/content/470/2166/20140063.full.pdf`, `doi:10.1098/rspa.2014.0063`.
URL `http://rspa.royalsocietypublishing.org/content/470/2166/20140063`

[4] A. Demma, P. Cawley, M. Lowe, A. Roosenbrand, B. Pavlakovic, The reflection of guided waves from notches in pipes: a guide for interpreting corrosion measurements, NDT & E International 37 (3) (2004) 167 – 180. `doi:https://doi.org/10.1016/j.ndteint.2003.09.004`.
URL `http://www.sciencedirect.com/science/article/pii/S0963869503001269`

[5] S. Fletcher, M. J. S. Lowe, M. Ratassepp, C. Brett, Detection of axial cracks in pipes using focused guided waves, Journal of Nondestructive Evaluation 31 (1) (2012) 56–64. `doi:10.1007/s10921-011-0120-x`.
URL `https://doi.org/10.1007/s10921-011-0120-x`

[6] C. Willey, F. Simonetti, P. Nagy, G. Instanes, Guided wave tomography of pipes with high-order helical modes, NDT & E International 65 (2014) 8 – 21. `doi:https://doi.org/10.1016/j.ndteint.2014.03.010`.
URL `http://www.sciencedirect.com/science/article/pii/S0963869514000449`

[7] J. Rao, M. Ratassepp, Z. Fan, Guided wave tomography based on full waveform inversion, IEEE Transactions on Ultrasonics, Ferroelectrics, and Frequency Control 63 (5) (2016) 737–745. `doi:10.1109/TUFFC.2016.2536144`.

[8] S. Rodriguez, M. Deschamps, M. Castaings, E. Ducasse, Guided wave topological imaging of isotropic plates, Ultrasonics 54 (7) (2014) 1880 – 1890. `doi:https://doi.org/10.1016/j.ultras.2013.10.001`.
URL `http://www.sciencedirect.com/science/article/pii/S0041624X13002862`

[9] C. Holmes, B. W. Drinkwater, P. D. Wilcox, Post-processing of the full matrix of ultrasonic transmit-receive array data for non-destructive evaluation, NDT & E International 38 (8) (2005) 701 – 711. `doi:http://dx.doi.org/10.1016/j.ndteint.2005.04.002`.
URL `http://www.sciencedirect.com/science/article/pii/S0963869505000721`

[10] L. L. Jeune, S. Robert, E. L. Villaverde, C. Prada, Plane wave imaging for ultrasonic non-destructive testing: Generalization to multi-modal imaging, Ultrasonics 64 (Supplement C) (2016) 128 – 138. `doi:https://doi.org/10.1016/j.ultras.2015.08.008`.

URL   http://www.sciencedirect.com/science/article/pii/
S0041624X15002188

[11] D. Colton, A. Kirsch, A simple method for solving inverse scattering problems in the resonance region, Inverse Problems 12 (1996) 383–393.

[12] T. Arens, Linear sampling methods for 2D inverse elastic wave scattering, Inverse Problems 17 (5) (2001) 1445–1464. `doi:10.1088/0266-5611/17/5/314`.
URL `http://dx.doi.org/10.1088/0266-5611/17/5/314`

[13] A. Charalambopoulos, D. Gintides, K. Kiriaki, The linear sampling method for non-absorbing penetrable elastic bodies, Inverse Problems 19 (3) (2003) 549–561. `doi:10.1088/0266-5611/19/3/305`.
URL `http://dx.doi.org/10.1088/0266-5611/19/3/305`

[14] D. Colton, H. Haddar, P. Monk, The linear sampling method for solving the electromagnetic inverse scattering problem, SIAM J. Sci. Comput. 24 (3) (2002) 719–731. `doi:10.1137/S1064827501390467`.
URL `http://dx.doi.org/10.1137/S1064827501390467`

[15] H. Haddar, P. Monk, The linear sampling method for solving the electromagnetic inverse medium problem, Inverse Problems 18 (3) (2002) 891–906. `doi:10.1088/0266-5611/18/3/323`.
URL `http://dx.doi.org/10.1088/0266-5611/18/3/323`

[16] Y. Xu, C. Mawata, W. Lin, Generalized dual space indicator method for underwater imaging, Inverse Problems 16 (6) (2000) 1761–1776.
URL `http://stacks.iop.org/0266-5611/16/i=6/a=311`

[17] A. Charalambopoulos, D. Gintides, K. Kiriaki, A. Kirsch, The factorization method for an acoustic wave guide, 7th Int. Workshop on Mathematical Methods in Scattering Theory and Biomedical Engineering (2006) 120–127.

[18] L. Bourgeois, E. Lunéville, The linear sampling method in a waveguide: a modal formulation, Inverse Problems 24 (1) (2008) 015018. `doi:10.1088/0266-5611/24/1/015018`.
URL `http://dx.doi.org/10.1088/0266-5611/24/1/015018`

[19] P. Monk, V. Selgas, Sampling type methods for an inverse waveguide problem, Inverse Problems and Imaging 6 (4) (2012) 709–747.

[20] L. Borcea, D.-L. Nguyen, Imaging with electromagnetic waves in terminating waveguides, Inverse Probl. Imaging 10 (4) (2016) 915–941. `doi:10.3934/ipi.2016027`.
URL `http://dx.doi.org/10.3934/ipi.2016027`

[21] F. Cakoni, D. Colton, The linear sampling method for cracks, Inverse Problems 19 (2) (2003) 279–295. `doi:10.1088/0266-5611/19/2/303`.
URL `http://dx.doi.org/10.1088/0266-5611/19/2/303`

[22] F. Ben Hassen, Y. Boukari, H. Haddar, Application of the linear sampling method to identify cracks with impedance boundary conditions, Inverse Probl. Sci. Eng. 21 (2) (2013) 210–234. doi:10.1080/17415977.2012.686997.
URL http://dx.doi.org/10.1080/17415977.2012.686997

[23] F. Pourahmadian, B. B. Guzina, H. Haddar, Generalized linear sampling method for elastic-wave sensing of heterogeneous fractures, Inverse Problems 33 (5) (2017) 055007, 32. doi:10.1088/1361-6420/33/5/055007.
URL http://dx.doi.org/10.1088/1361-6420/33/5/055007

[24] Q. Chen, H. Haddar, A. Lechleiter, P. Monk, A sampling method for inverse scattering in the time domain, Inverse Problems 26 (8) (2010) 085001, 17. doi:10.1088/0266-5611/26/8/085001.
URL http://dx.doi.org/10.1088/0266-5611/26/8/085001

[25] P. Monk, V. Selgas, An inverse acoustic waveguide problem in the time domain, Inverse Problems 32 (5) (2016) 055001.
URL http://stacks.iop.org/0266-5611/32/i=5/a=055001

[26] V. Baronian, L. Bourgeois, A. Recoquillay, Imaging an acoustic waveguide from surface data in the time domain, Wave Motion 66 (2016) 68–87. doi:10.1016/j.wavemoti.2016.05.006.
URL http://dx.doi.org/10.1016/j.wavemoti.2016.05.006

[27] L. Bourgeois, S. Fliss, On the identification of defects in a periodic waveguide from far field data, Inverse Problems 30 (9) (2014) 095004, 31.
URL https://doi.org/10.1088/0266-5611/30/9/095004

[28] H. Brezis, Functional analysis, Sobolev spaces and partial differential equations, Universitext, Springer, New York, 2011.

[29] A. Recoquillay, Méthodes d'échantillonnage appliquées à l'imagerie de défauts dans un guide d'ondes élastiques, Ph.D. thesis, Paris Saclay (2018).
URL http://www.theses.fr/2018SACLY001

[30] V. Baronian, A. S. Bonnet-Ben Dhia, E. Lunéville, Transparent boundary conditions for the harmonic diffraction problem in an elastic waveguide, J. Comput. Appl. Math. 234 (6) (2010) 1945–1952. doi:10.1016/j.cam.2009.08.045.
URL http://dx.doi.org/10.1016/j.cam.2009.08.045

[31] W. B. Fraser, Orthogonality relation for the Rayleigh-Lamb modes of vibration of a plate, J. Acoust. Soc. Am. 59 (1976) 215–216.

[32] V. Pagneux, A. Maurel, Lamb wave propagation in elastic waveguides with variable thickness, Proc. R. Soc. Lond. Ser. A Math. Phys. Eng. Sci. 462 (2068) (2006) 1315–1339. doi:10.1098/rspa.2005.1612.
URL http://dx.doi.org/10.1098/rspa.2005.1612

[33] V. Baronian, Couplage des méthodes modale et éléments finis pour la diffraction des ondes élastiques guidées, Ph.D. thesis, Ecole Polytechnique (2009).

[34] L. Bourgeois, E. Lunéville, The linear sampling method in a waveguide: a formulation based on modes, Journal of Physics: Conference Series 135 (2008) 012023.

[35] D. Colton, M. Piana, R. Potthast, A simple method using Morozov's discrepancy principle for solving inverse scattering problems, Inverse Problems 13 (1997) 1477–1493.

[36] A. Moitra, Super-resolution, extremal functions and the condition number of Vandermonde matrices, in: STOC'15—Proceedings of the 2015 ACM Symposium on Theory of Computing, ACM, New York, 2015, pp. 821–830.

[37] A. Imperiale, S. Chatillon, P. Calmon, N. Leymarie, S. Imperiale, E. Demaldent, UT Simulation of Embedded Parametric Defects Using a Hybrid Model Based Upon Spectral Finite Element and Domain Decomposition Methods, Proceedings of the 19th World Conference on Non-Destructive Testing.

[38] K. Jezzine, Approche modale pour la simulation globale des contrôles non-destructifs par ondes élastiques guidées, Ph.D. thesis, Université Bordeaux 1 (2006).

[39] D. Royer, E. Dieulesaint, Ondes élastiques dans les solides, Interaction of Mechanics and Mathematics, Masson, Paris, 1996, tome 1, Propagation libre et guidée.